# A systematic mapping procedure based on the Modified Gaussian Model to characterize magmatic units from olivine/pyroxenes mixtures: Application to the Syrtis Major volcanic shield on Mars

Harold Clenet, Patrick Pinet, Georges Ceuleneer, Yves Daydou, Frédérick Heuripeau, Christine Rosemberg, Jean-Pierre Bibring, Giancarlo Bellucci, Francesca Altieri, Brigitte Gondet

JOURNAL OF GEOPHYSICAL RESEARCH: PLANETS, VOL. 118, 1632–1655, doi:10.1002/jgre.20112, 2013

# A systematic mapping procedure based on the Modified Gaussian Model to characterize magmatic units from olivine/pyroxenes mixtures: Application to the Syrtis Major volcanic shield on Mars

Harold Clenet,[1,2,3] Patrick Pinet,[1,2] Georges Ceuleneer,[4,5] Yves Daydou,[1,2] Frédérick Heuripeau,[1,2] Christine Rosemberg,[1,2] Jean-Pierre Bibring,[6] Giancarlo Bellucci,[7] Francesca Altieri,[7] and Brigitte Gondet[6]

Received 3 April 2013; revised 8 July 2013; accepted 10 July 2013; published 22 August 2013.

[1] Clenet et al. (2011) have developed an adapted version of the Modified Gaussian Model (MGM). The improvements allow the characterization of spectra of olivine-pyroxene(s) mixtures, addressing both modal composition and individual minerals chemical composition. This version of MGM is fully automated and operational with large amounts of hyperspectral imaging data. Two natural cases are considered. The first one is the Sumail massif in the Oman ophiolite (Earth). Based on our approach applied to HyMap data, two contrasted lithologic units are mapped: the mantle, which is harzburgite dominated, and the crust made of gabbros and clinopyroxene-rich cumulates, with spectral variations interpreted in terms of pyroxenes chemical compositions. Once this new MGM mapping approach has been validated on a controlled natural situation, we map the distribution of mafic assemblages across the Syrtis Major volcano on Mars using a visible and near-infrared (VNIR) - short wave infrared (SWIR) Observatoire pour la minéralogie, l'eau, les glaces et l'activité (OMEGA) / Mars Express (MEx) mosaic. Our results are in agreement with previous work but olivine appears to be more abundant than previously estimated in the central part of the volcanic edifice, especially in ternary mafic assemblages (augite, olivine, enstatite). Based on these results, we propose a possible scenario for the igneous (and thus thermal) evolution of the Syrtis Major region. Surrounding terrains have formed first and local heterogeneity can be observed between northern and southern areas of the Noachian crust. We also observe variations in the mineral assemblages within Syrtis Major lavas, which can be interpreted in terms of differentiation from a common parent melt and/or of a progressive evolution of the mantle source composition and temperature.

**Citation:** Clenet, H., et al. (2013), A systematic mapping procedure based on the Modified Gaussian Model to characterize magmatic units from olivine/pyroxenes mixtures: Application to the Syrtis Major volcanic shield on Mars, *J. Geophys. Res. Planets*, *118*, 1632–1655, doi:10.1002/jgre.20112.

## 1. Introduction

[2] Mafic minerals have been detected early in the exploration of Mars, first using telescopic observations [e.g., *Adams*, 1968; *Pinet and Chevrel*, 1990]. The Syrtis Major region is characterized by one of the darkest albedos on Mars and low dust cover and exhibits strong absorption features indicative of the widespread occurrence of mafic minerals and variability within the volcanic construct [e.g., *Pinet and Chevrel*, 1990]. Telescopic detections have been confirmed by orbital observations using different techniques such as thermal infrared [e.g., *Bandfield*, 2002; *Bandfield et al*., 2000] or visible near-infrared optical spectroscopy [e.g., *Mustard and Sunshine*, 1995; *Bibring and Erard*, 2001; *Mustard et al*., 2005; *Poulet et al*., 2007; *Ody et al*., 2012].

[3] Another way to understand Martian petrology relies on SNC meteorites [*McSween*, 1994]. Detailed studies of their constituents can be done, especially in terms of minerals chemical composition [e.g., *McCoy et al*., 1992; *Mittlefehldt*, 1994; *Smith and Hervig*, 1979; *Stolper and McSween*, 1979]. Crystallization conditions can then be inferred from the pyroxenes composition [*Lindsley*, 1983]. However, direct comparison between SNCs analyses and remote-sensing observations is hard to establish. Indeed, on the one hand, the loci of origin of the meteorites are not clearly known

[1]Université de Toulouse, UPS-OMP, IRAP, Toulouse, France.
[2]CNRS, IRAP, Toulouse, France.
[3]Now at Earth and Planetary Science Laboratory, Ecole Polytechnique Fédérale de Lausanne, Lausanne, Switzerland.
[4]Université de Toulouse, UPS-OMP, GET, Toulouse, France.
[5]CNRS, GET, Toulouse, France.
[6]Institut d'Astrophysique Spatiale, Université Paris-Sud, Orsay, France.
[7]IAPS, Istituto Nazionale di Astrofisica, Rome, Italy.

Corresponding author: H. Clenet, Earth and Planetary Science Laboratory, Ecole Polytechnique Fédérale de Lausanne, Station 3, CH-1015 Lausanne, Switzerland. (harold.clenet@epfl.ch)


2169-9097/13/10.1002/jgre.20112

[*Mustard and Sunshine*, 1995; *Hamilton et al*., 2003], and on the other hand, the chemical composition of the Martian mafic minerals is not well constrained from remote sensing, despite recent efforts [e.g., *Bibring et al*., 2005; *Combe et al*., 2008; *Kanner et al*., 2007; *Poulet et al*., 2007].

[4] The transition between the Noachian and Hesperian epochs on Mars is characterized by fundamental changes in planetary-scale processes, including a potential increase in volcanic activity [e.g., *Baratoux et al*., 2011; *Bibring et al*., 2006; *Greeley and Spudis*, 1981; *Hiesinger and Head*, 2004]. The global change in igneous mineralogies observed on the surface could be explained by an evolution of the mantle composition and thermal structure and, consequently, of the partial melting and crystallization conditions [*Baratoux et al*., 2013]. The chemical composition of each mafic mineral on the surface is related to the igneous processes which have affected the planet through time. Thus, detection of olivines and pyroxenes and characterization of their respective composition are instrumental in documenting the magmatic evolution of Mars.

[5] The aim of this paper is focused toward better constraining Mars igneous processes in the region of Syrtis Major using recent developments from *Clenet et al*. [2011]. Improvement in data processing now allows us characterizing olivine and pyroxene chemical composition within their solid solution (respectively forsterite-fayalite and enstatite-ferrosilite-diopside-hedenbergite), even in the case of complex mixtures involving both minerals. In the first part of the paper, we illustrate the validation process from laboratory data to controlled geologic mapping based on imaging spectroscopy under natural conditions on Earth. This demonstration was made by means of an airborne hyperspectral survey performed over a massif of the Oman ophiolite, for which ground truth (e.g., rocks modal abundance and minerals chemical composition) is available through extensive field and petrologic work. In the second part of the paper, we apply the same method to an integrated VNIR-SWIR OMEGA/MEx mosaic produced over the volcanic shield of Syrtis Major and propose a first global depiction of the regional compositional changes associated with the identified mafic assemblages.

## 2. Olivine and Pyroxenes Spectroscopy

[6] In visible and near-infrared reflectance spectra, olivine and pyroxenes are characterized by their $Fe^{2+}$ electronic transition absorption bands. For a perfect octahedral crystal field, the electronic transition creates an absorption feature with minima around 1.10 μm. However, absorptions of a same metallic ion can occur at different wavelengths because of variations in the crystallographic site symmetry, bond type and length, and site distortion [*Burns*, 1993; *Sunshine and Pieters*, 1998; *Klima et al*., 2011], and absorption width is linked to thermal vibrations that modify the bond length around a mean value [*Burns*, 1993].

[7] Consequently, pyroxenes reflectance spectra show two main absorptions respectively around 1 and 2 μm and a less pronounced absorption at 1.2 μm [*Hunt and Salisbury*, 1970; *Adams*, 1974, 1975; *Singer*, 1981; *Klima et al*., 2007]. This 1.2 μm absorption is the result of molecular distortion in the $M_1$ crystallographic site [*Burns*, 1993]. Spectra of olivine are dominated by a broad complex absorption feature which is a composite of several absorptions: two of them correspond to iron in the $M_1$ site (around 0.85 and 1.25 μm) while the third one, around 1.05 μm, corresponds to the $M_2$ site [*Burns*, 1970; *Hunt*, 1977; *Sunshine and Pieters*, 1998; *Dyar et al*., 2009].

[8] The substitution of different-sized cations, such as calcium, iron, and magnesium, also controls the positions of the different absorptions minima. In the case of olivine [$(Mg,Fe)_2SiO_4$], solid solution ranges from forsterite to fayalite. The overall position of the 1.0 μm absorption feature is known to shift toward longer wavelengths with increasing iron content [*Burns*, 1970, 1993; *Adams*, 1975; *King and Ridley*, 1987]. For pyroxenes [$(Ca,Mg,Fe)_2Si_2O_6$], wavelengths shift is a function of Fe/(Mg + Fe + Ca) ratio [*Adams*, 1974, 1975; *Cloutis et al*., 1986; *Cloutis and Gaffey*, 1991b]. Basically, enstatite (orthopyroxene) main absorptions occur around 0.90 and 1.85 μm, while diopside (clinopyroxene) main absorptions occur around 1.00 and 2.30 μm [*Hunt and Salisbury*, 1970; *Adams*, 1974, 1975; *Singer*, 1981]. The difference between the two types of pyroxenes is related to $Fe^{2+}$ position: Metallic ion is located preferentially in $M_2$ site for orthopyroxene and in $M_1$ site for clinopyroxene, $Ca^{2+}$ being in $M_2$ site in the second case [*Adams*, 1974; *Burns*, 1993]. *Hazen et al*. [1978], followed by *Cloutis and Gaffey* [1991a], have shown that absorption features evolve progressively between the pyroxenes end-member, absorption minima shifting to longer wavelength with increasing Fe content (diopside to hedenbergite and enstatite to ferrosilite) and Ca content (enstatite-pigeonite-augite-diopside).

[9] In this paper, we will use the terms orthopyroxene and clinopyroxene (respectively OPX and CPX) with reference to the minerals structures when known and to their corresponding MGM initial configurations (see next section). We will also use the terms low-calcium pyroxene and high-calcium pyroxene (respectively LCP and HCP) with reference to pyroxene compositions. LCP and HCP encompass respectively the enstatite-ferrosilite-pigeonite and the augite-diopside-hedenbergite range of compositions.

## 3. Implementation of a MGM-Based Mineralogical Mapping Procedure

[10] The quantitative interpretation of mineralogy from spectra is limited as it is hampered by the overlap of the absorption features, particularly when there is a mixture of two or three minerals, as it is frequently the case with rocks. Indeed, such spectra show intermediate characteristics to those of the different end-member components. Those properties vary nonlinearly as a function of minerals relative abundance and composition [*Adams*, 1974; *Singer*, 1981; *Cloutis and Gaffey*, 1991b; *Sunshine and Pieters*, 1998]. The Modified Gaussian Model (MGM), developed by *Sunshine et al*. [1990] and *Sunshine and Pieters* [1993, 1998], has been a first step to detect and resolve these end-member contributions. MGM technique aims at deconvolving overlapping absorptions of mafic mineral spectra into their fundamental absorption components. It is achieved by considering a sum of modified Gaussian functions characterized by their band centers, widths, and strengths. The specific aim of this model is to directly account for electronic transition processes [*Sunshine et al*., 1990].

[11] However, as demonstrated by *Kanner et al*. [2007] and *Clenet et al*. [2011], MGM results are sensitive to the initial parameters (i.e., centers, widths, and strengths) and thus

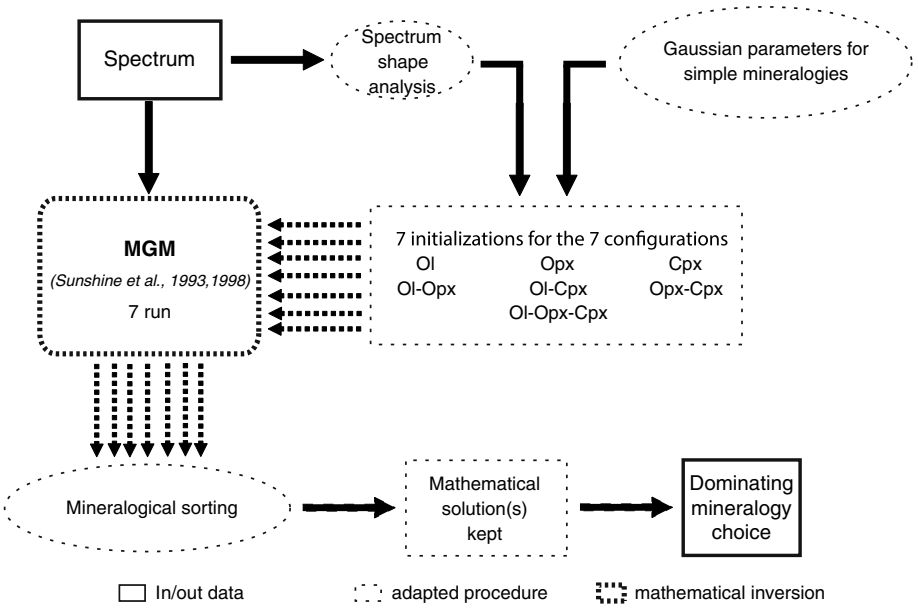


**Figure 1.** Schematic of fitting process used for each spectrum from *Clenet et al*. [2011]. Parameters for modified Gaussian of simple mineralogies are extracted from literature [*Adams*, 1974; *Sunshine and Pieters*, 1993, 1998] and set as fixed inputs. All the process is fully automated and the mathematical inversion is the one used by *Sunshine and Pieters* [1993, 1998]. The output products are mathematical solutions, which are validated in terms of spectral consistency [*Clenet et al*., 2011].

MGM cannot simply be implemented blindly on an entire data set as acquired on planetary surfaces. An automatic procedure has been recently implemented by *Clenet et al*. [2011] based on the original MGM approach [*Sunshine et al*., 1990; *Sunshine and Pieters*, 1993] in order to deal with unknown mafic mineralogy in the case of laboratory or natural rock spectra. A key issue is to initialize the MGM procedure with a proper setting for the parameters. Consequently, an automatic analysis of the shape of the spectrum is first performed (spectrum maxima and minima are used to estimate at first-order absorption strengths and widths). The continuum is handled with a second-order polynomial initially adjusted on the local maxima along the spectrum (curvature, slope, and shift are free to move during the modeling). *Clenet et al*. [2011] consider all the mixture possibilities involving orthopyroxene, clinopyroxene, and olivine and use accordingly for each of the seven configurations different numbers of Gaussians (from 3 to 7), depending on the potential complexity of the mixture. Additional Gaussians centered around 0.5 (UV charge-transfer absorption) and 0.6 (ferric absorption) and at 1.4, 1.9, and 2.3 μm (hydration and alteration effects) may be requested to account for spectral features not related to mafic mineralogy. Gaussians parameters initial settings for the seven configurations are made each time on the basis of the spectrum shape and the laboratory results available in the literature in the case of simple mixtures of mafic minerals (see *Clenet et al*. [2011] for details). Considering all the mixture possibilities with the three mafic components, MGM modeling is run seven times, with seven different initializations, on a given spectrum. Root-mean-square (RMS) residuals cannot be used as the only parameter to check for the validity of the results as large number of Gaussian functions may result in low RMS mathematical solutions without any physical meaning. Consequently, the returned MGM solutions are then assessed on the basis of a mineralogical sorting (i.e., each modeled Gaussian function must verify the spectroscopic criteria defined in the literature [*Adams*, 1974; *Sunshine and Pieters*, 1993, 1998]) and are accordingly either validated or discarded. Finally, the solution(s) kept is (are) interpreted in terms of mineralogy [*Clenet et al*., 2011]. A sketch illustrating the process is presented in Figure 1.

[12] The results presented in *Clenet et al*. [2011] show that this new MGM approach is able to model simple and complex mafic mineralogies, including binary and ternary mixtures (involving orthopyroxene, spectral type B clinopyroxene, and olivine) for a large range of grain sizes. It is a quantitative step forward to characterize both modal and chemical compositions of pyroxenes and olivines. A demonstration of the methodology on specific examples of binary and ternary olivine-pyroxenes mixtures has been made (with and without plagioclase), which shows that the different nonlinear effects which affect the Gaussian parameters (center and strength) can be successfully handled. One of the major advantages of this approach is that band center positions associated with the different mafic minerals are not set in the inverse problem, and thus the MGM outputs are truly informative of the chemical composition of pyroxenes and olivines. With the consideration of some limits on the detection thresholds, these results set confidence on the operational use of the Modified Gaussian Model with large hyperspectral data sets, for establishing detailed lithological/mineralogical mappings intended to explore the petrology and mode of emplacement of magmatic units.

## 4. Validation of the Mapping Procedure on the Oman's Ophiolite

[13] The Oman ophiolite is a remnant of the vanished Tethys Ocean [*Glennie et al*., 1974]. Due to the convergence

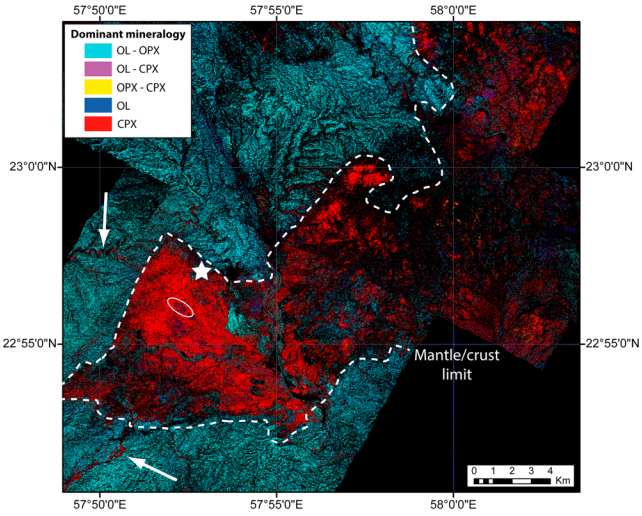


**Figure 2.** Map of dominant mineralogy. Two distinct units are clearly mapped: The red pixels are rocks that are dominated by clinopyroxene, i.e., clinopyroxene (with plagioclase) which are in gabbros (crustal section), while the cyan pixels are olivine and orthopyroxene, i.e., harzburgite (mantle section). The dashed line represents the limit between the crustal and the mantle sections and matches the limits as defined using the geological map. The white star indicates the outcrop from which sample analyses are represented in Figure 3. The white arrows point out gabbros originating from outcrops of the crustal section and transported downslope along wadi. OL-CPX, OPX-CPX, and OL detections can also be found within the studied area but only in outcrops with small spatial extents. The white ellipse corresponds to local wehrlite-rich patches.

between the Arabian and Eurasian plates, an ~30,000 km$^2$ chunk of the Tethysian lithosphere, including mantle peridotites and the overlying mafic crust, was thrust on the Oman continental margin in Maastrichtian time (~70 Ma). The recent (a few Ma) uplift of the Oman mountains led to the exposure of the ophiolite. Thanks to present-day arid conditions and to the fact that the Oman ophiolite presents large outcrops of relatively homogenous lithologies, this area is quite appropriate for developing hyperspectral remote-sensing methods relevant to the study of planetary surfaces [cf. *Clenet et al*., 2010; *Combe et al*., 2006; *Roy et al*., 2009].

[14] The Sumail massif and the Maqsad oasis are located in the southeastern part of the Oman ophiolite, where a former mid-ocean ridge axis and the related mantle upwelling (the Maqsad "diapir") have been mapped through the study of high-temperature plastic deformation structures in mantle harzburgites [*Ceuleneer et al*., 1988; *Ceuleneer*, 1991]. The evolution of the thermal structure of the Maqsad diapir and of the magma source during its emplacement at shallow mantle depth has been constrained by detailed petrological studies and by numerical modeling [*Ceuleneer et al*., 1996; *Benoit et al*., 1999; *Python and Ceuleneer*, 2003; *Rabinowicz and Ceuleneer*, 2005; *Clenet et al*., 2010].

[15] The primary igneous mineralogy in the different units cropping out in the Sumail massif is controlled by olivine/pyroxenes (both HCP and LCP) and plagioclase mixtures. Accordingly, this area presents valuable spectroscopic analogies with low-albedo Martian terrains such as Syrtis Major.

[16] Several geological maps of the Sumail massif have been published during the last decades. The map by *Glennie et al*. [1974] covers all of the Oman Mountains at a 1:500,000 scale. Following this pioneering work, the BRGM (French Geological Survey) has produced more detailed maps, at a 1:100,000 scale, of the central part of the ophiolite, including the Sumail massif [*Rabu et al*., 1986; *Villey et al*., 1986]. *Amri* [1995] produced a detailed map at a 1:40,000 scale that represented a significant improvement in the definition and mapping of the different lithological units making up the crustal section of the Sumail massif.

### 4.1. HyMap

[17] Hyperspectral images of the Sumail Massif were acquired by the HyMap airborne imaging spectrometer on 4 and 6 December 2002 [*Pinet et al*., 2003]. The solar elevation ranges from 35° to 45° while azimuth ranges between 150° and 220°. HyMap is a 128-channel instrument that collects data between 0.45 and 2.48 µm with a spectral resolution of 15–20 nm [*Cocks et al*., 1998]. Spectral coverage is nearly continuous except for the 1.40 and 1.90 µm bands that are saturated by atmospheric water vapor. HyMap data have been atmospherically corrected by the HyVista Corp. on the basis of atmosphere removal radiative transfer model [*CIRES*, 1999; *Gao et al*., 1993] and the Empirical Flat Field Optimal Reflectance Transformation [*Boardman*, 1998]. Geometry corrections and orthorectification are based on an Advanced Spaceborne Thermal Emission and Reflection Radiometer digital elevation model. A cross-track correction was also applied to obtain a spectrally homogeneous mosaic (each band is divided by a function which is representative of the reflectance evolution orthogonally to the trace axis).

[18] The data set covers an ~15 × 60 km$^2$ area with a pixel size of about 6 m acquired at 3500–4000 m flight elevation (i.e., 4 km wide swath). In order to generate a large mapping coverage with the highest quality, an extended mosaic was built using images with the lowest amount of cloud cover and shadows. The HyMap mosaic overlaps the regional geological cartography established by *Amri* [1995] and shows that both the mantle (essentially harzburgitic) and the crustal sections (essentially gabbroic) of the massif have been surveyed. The mosaic has already been used to map distinct lithological units and highlight specific lithologies [*Combe et al*., 2006; *Pinet et al*., 2006; *Clenet et al*., 2008, 2010; *Roy et al*., 2009].

[19] As a detailed study of Oman's ophiolite using remote sensing is not the aim of this work, we rather focus our tests only on a small subset of the mosaic. The selected area is nevertheless representative of the whole geological diversity of the region (see Figure 2).

### 4.2. Spectral Mapping of Lithological Units

[20] Working with a terrestrial case allowed us to use both sampling and field spectroscopy techniques to establish a ground truth database and validate our interpretation of HyMap observations. As described in *Clenet et al*. [2011] when absorptions features are too weak, the MGM may return mathematical solutions which do not reflect the real mineralogy. Consequently, prior to any systematic analysis on the whole HyMap data set, we test each pixel in order to

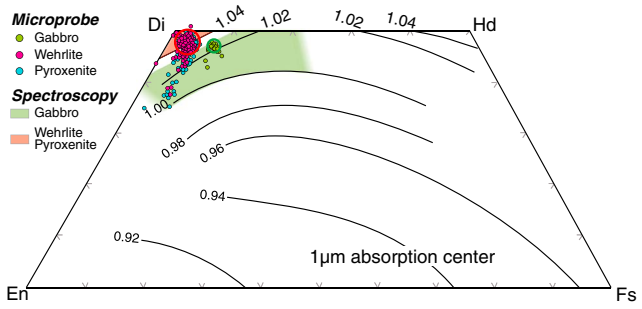


**Figure 3.** Clinopyroxene compositions from the outcrop studied intensively in *Clenet et al*. [2010] (see Figure 3 therein for a picture of the outcrop). The red field corresponds to the chemical compositions estimated using spectroscopy on HyMap data set for clinopyroxene/wehrlite. Similarly, green field corresponds to layered gabbros compositions. Fifty-three samples have been taken along the section. Composition of ~750 clinopyroxene grains has been determined using an SX50 electron microprobe (see *Clenet et al*. [2010] for analytical conditions) and each measurement is reported in the quadrilateral as a colored dot (red, blue, and green, respectively, for each considered unit). Red and green circles indicate the highest density of data for diopsides and augites respectively.

discard the featureless spectra. On the HyMap mosaic, the strength of the absorption features has a large range of values, going from spectra with very shallow to deep absorption features similar to those observed on laboratory data. The featureless spectra are found mainly in wadi (i.e., dry valleys) and oases and on recent sedimentary deposits. Once this filtering has been done, the MGM is automatically initialized and run seven times with the different configurations on the whole data set, each pixel being processed independently. Seven mathematical solutions are obtained for each pixel (i.e., seven mosaics are calculated). Prior to any mineralogical analysis, we check the global fit quality of each of the seven solutions with the RMS. Following *Chabrillat et al*. [2000], a rejection threshold is set: For each solution, pixels that present RMS values above the mean RMS of the mosaic increased by 2 times the standard deviation are rejected. As no preprocessing on the mosaic is done, pixels associated with either vegetation, a pronounced amount of shadow, and/or clouds/haze are removed. Depending on the considered configuration, this step may discard up to 8% of the whole mosaic.

[21] The final step before interpretation of MGM results in terms of mineralogy consists of a mineralogical sorting. Each mathematical solution is independently tested to assess that Gaussian functions parameters are physically meaningful (see section 3) [*Clenet et al*., 2011]. In the most general case, only one configuration per pixel is kept after this process. However, a few pixels located in the western part of the massif (i.e., in the harzburgite unit) are modeled correctly with the two following configurations: olivine and olivine-orthopyroxene. Interestingly, optical microscopy on samples picked up from these pixels has confirmed that for those rocks, olivine is the dominant mineral (olivine crystals represent ~85% of the whole rock) in an orthopyroxene-olivine mixture. Earlier tests [*Clenet et al*., 2011] have shown that in this case, the olivine-orthopyroxene configuration is returned.

[22] The resulting mineralogical mapping is presented in Figure 2 and shows that our MGM systematic procedure correctly detects the main lithological units. Cyan pixels, associated with an olivine-orthopyroxene mixture, are dominant on the western part of the mosaic where mantle harzburgites have been mapped. Trending north-east southwest, a stripe of blue pixels is found in the mantle unit. It is indicative of variations in the olivine/orthopyroxenes ratio in the harzburgite unit. Field observations confirm that this blue stripe is depleted in orthopyroxenes relative to the average harzburgites of the mosaic [*Clenet*, 2009]. Red pixels, associated with clinopyroxene-rich lithologies (essentially gabbros), are reported mainly on the eastern part of the mosaic mapped as the crustal section of the Sumail massif. The ability of our procedure to detect subtle geological features is illustrated in Figure 2. The sinuous red strings (white arrows) in the mantle harzburgites enhance the contours of those wadi that are filled with gabbro block transported from the crustal section located uphill in this area. Purple pixels, associated with the occurrence of olivine and clinopyroxene minerals, are found in the crustal section. They correspond to wehrlite-rich outcrops (e.g., see white ellipse). The mantle/crust boundary is correctly delineated and is successfully propagated outward the geological map of *Amri* [1995]. The alteration of the primary igneous minerals (mostly serpentinization of olivine) and the desert varnish are potential sources of ambiguities and may generate false detections. In spite of this, it appears that mineral assemblages including olivine and pyroxenes are correctly detected and largely agree with field observation. Moreover, it has led to the detection of clinopyroxene-rich cumulates (interlayered clinopyroxenites and wehrlites) whose occurrence was previously undocumented [*Clenet et al*., 2010]. An extensive discussion on the geological implications of these results is beyond the scope of the present work and will be addressed in a separate paper.

### 4.3. Local Variations in Pyroxenes Chemical Compositions

[23] Two clinopyroxene (HCP) types with slightly different compositions have been detected in the area surveyed by HyMap (white star in Figure 2) and have been used as ground truth for our detections. For this purpose, we collected 53 samples along a 200 m thick section of interlayered wehrlitic and pyroxenitic cumulates overlain by layered gabbroic cumulates. Mineral composition (major and minor elements) was determined with the electron microprobe [*Clenet et al*., 2010].

[24] A direct comparison with our spectroscopic results is done in the pyroxenes quadrilateral (Figure 3). The two trends we observe in HyMap data correspond to two different clinopyroxene compositions: Clinopyroxenes in pyroxenites and wehrlites plot in the field of diopside (high Mg/Fe ratio) while clinopyroxenes from gabbros have slightly lower Mg/Fe ratios and plot in the field of augites. This fits particularly well with the two fields defined using MGM results. Uncertainties inherent to visible near-infrared spectroscopy do not allow us to discriminate augites from diopsides with a low-Ca content (Figure 3). As a matter of fact, diopsides from werhlites and clinopyroxenites show a trend toward low-Ca composition. This scatter in the microprobe data is a classical

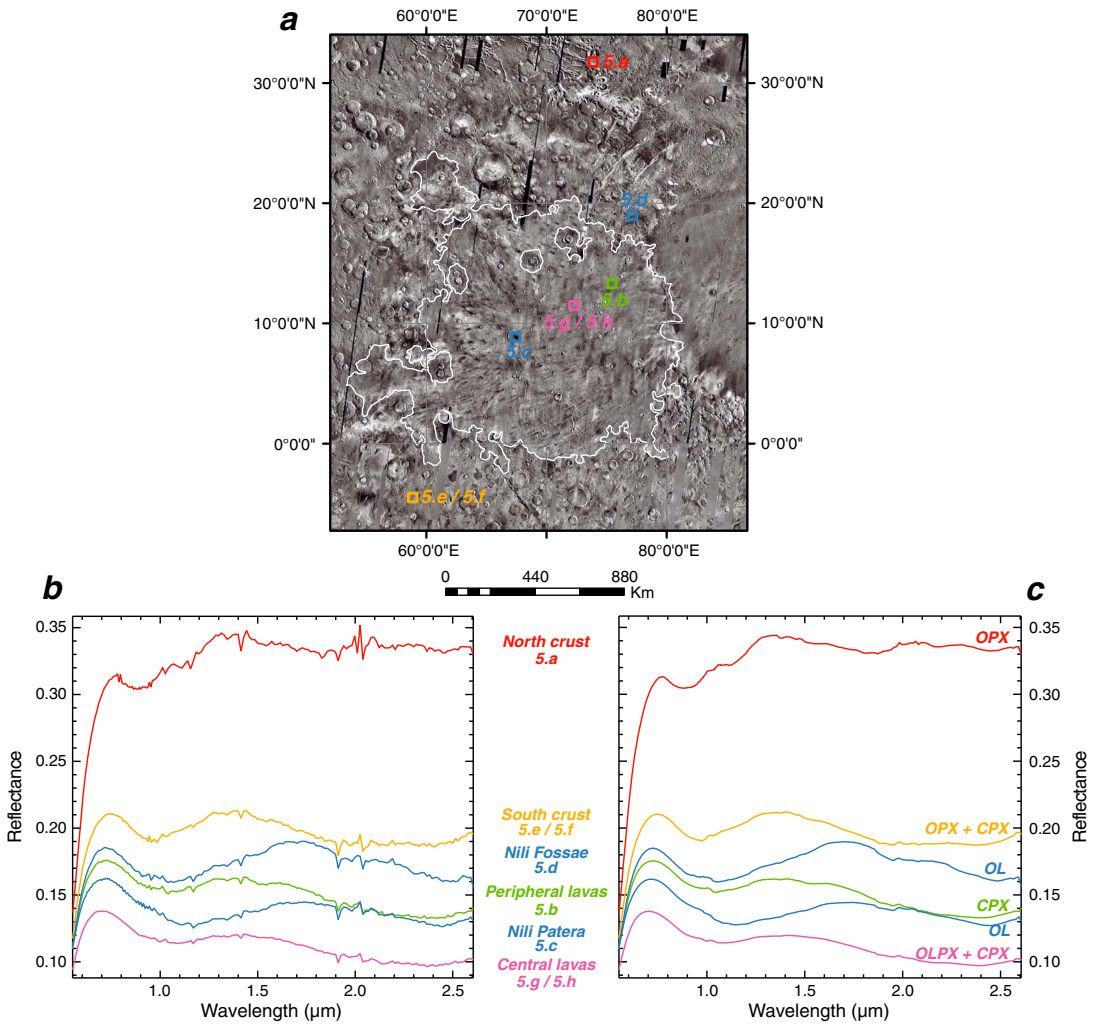


**Figure 4.** Collection of six OMEGA spectra representative of the spectral variability across the mosaic. The white line outlines the limit of the Syrtis Major edifice and the location of spectra is indicated by colored boxes on the map (Figure 4a) and displayed in reflectance below (Figure 4b). Labels 5x refer to the associated results presented in Figure 5. Spectra show high-frequency residual artefacts (atmospheric effects, VNIR-SWIR transition, etc.). The red and orange spectra are respectively representative of the north and south crust; the blue spectra correspond respectively to Nili Patera and Nili Fossae areas; the green spectrum corresponds to the peripheral lavas of Syrtis Major; the pink spectrum corresponds to the central lavas of the edifice. After applying a spectral smoothing (seven-channel sliding window; Figure 4c), the MGM is applied to each spectrum for the seven configurations. The best solution is plotted in Figure 5.

effect of submicron exsolutions of enstatite (LCP) in diopsides (HCP). It does not significantly affect the bulk composition of diopside grains as attested by the fact that ~50 analyses only among a total of 750 plot outside the red circle. Given the large pixel size, and the low abundance of exsolution, the average spectroscopic signal is not sensitive to this scatter in composition revealed by the in situ microprobe analyses.

[25] Oman data show that one can reliably make use of the proposed MGM-based mapping procedure for revealing and highlighting large-scale variations in pyroxene compositions from hyperspectral imaging observations acquired under natural conditions. This is of particular interest for orbital imaging spectroscopy used in planetary exploration of mafic terrains, like the Syrtis Major volcanic shield on Mars.

## 5. The Syrtis Major Volcanic Shield

[26] The Syrtis Major region on Mars lies near the boundary between the northern plains and the older highlands, near the Isidis impact structure. This circular large dome has been early recognized as a volcanic shield with two calderas, Nili Patera and Nili Meroe [*Schaber*, 1982]. Its surface morphology is dominated by lava flows intersected by compressive ridges. The end of the volcanic activity is Hesperian in age [*Hartmann and Neukum*, 2001; *Hiesinger and Head*, 2004]. Later erosion processes have occurred since that time [*Skok et al.*, 2010a].

[27] Detection of mafic materials has been made both from telescopic [e.g., *Bell et al.*, 1997; *Pinet and Chevrel*, 1990] and orbital observations [e.g., *Mustard et al.*, 1993, 2005]. Lavas have been found to be composed of pyroxenes, mainly

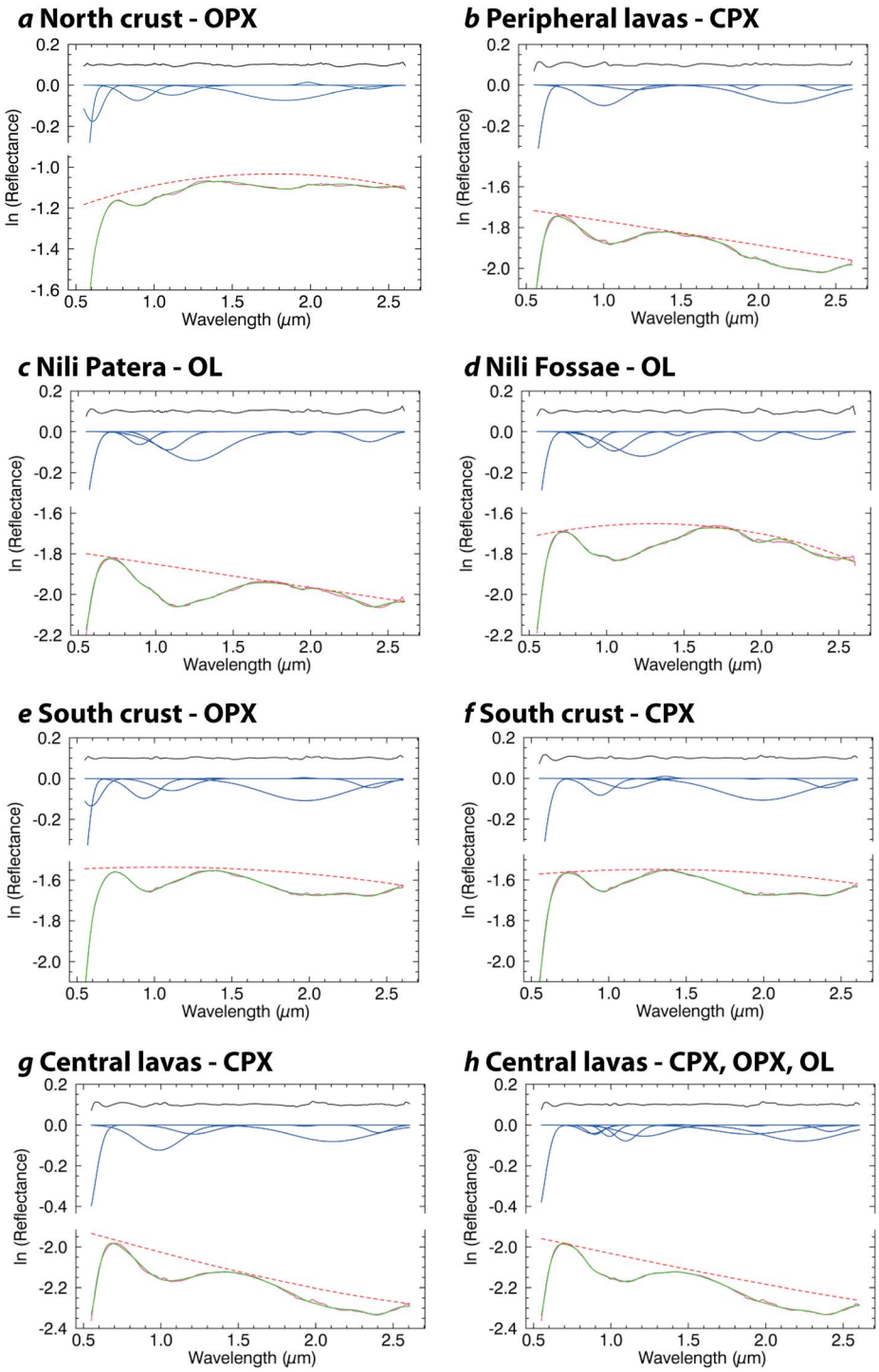


**Figure 5.** Results of the MGM deconvolution, considering different initial configurations, applied on the six spectra displayed in Figure 4. Shown on each graph are the measured spectrum (dotted pink line), the MGM modeled spectrum (displayed in green), the Gaussians and polynomial determined by the MGM deconvolution, and the residual error as a function of wavelength. Gaussians are displayed with a solid blue line. Dashed red line corresponds to the continuum modeled as a second-order polynomial. For clarity, the residuals (observed-modeled quantity) are shifted by +0.1. (a) The north crust spectrum, modeled by an orthopyroxene/ferric configuration. (b) The peripheral lavas spectrum, modeled by a clinopyroxene configuration. (c) The Nili Patera spectrum, modeled by an olivine configuration. (d) The Nili Fossae spectrum, modeled by an olivine configuration. (e) The south crust spectrum, modeled by an orthopyroxene configuration. (f) The south crust spectrum, modeled by a clinopyroxene configuration. (g) The central lavas spectrum, modeled by a clinopyroxene configuration. (h) The central lavas spectrum, modeled by a ternary configuration (orthopyroxene, clinopyroxene and olivine).

**Table 1.** Parameters Obtained Using Our MGM Procedure on the Six Particular Spectra Described in Figure 5[a]

| Spectrum | North Crust | | | South Crust | | | Nili Fossae | | | Nili Patera | | | Syrtis Peripheral Lavas | | |
|---|---|---|---|---|---|---|---|---|---|---|---|---|---|---|---|
| Mineral | Center | Width | Strength | Center | Width | Strength | Center | Width | Strength | Center | Width | Strength | Center | Width | Strength |
| Olivine | | | | | | | 888 | 154 | −0.08 | 896 | 162 | −0.06 | | | |
| | | | | | | | 1049 | 231 | −0.09 | 1079 | 220 | −0.09 | | | |
| | | | | | | | 1227 | 437 | −0.01 | 1250 | 457 | −0.14 | | | |
| LCP | 893 | 211 | −0.07 | 934 | 219 | −0.10 | | | | | | | | | |
| | 1117 | 278 | −0.05 | 1114 | 283 | −0.06 | | | | | | | | | |
| | 1835 | 619 | −0.07 | 1973 | 631 | −0.11 | | | | | | | | | |
| HCP | | | | | | | | | | | | | 1002 | 310 | −0.10 |
| | | | | | | | | | | | | | 1198 | 298 | −0.02 |
| | | | | | | | | | | | | | 2184 | 573 | −0.09 |
| Continuum | $Ax^2$ | $Bx$ | $C$ | $Ax^2$ | $Bx$ | $C$ | $Ax^2$ | $Bx$ | $C$ | $Ax^2$ | $Bx$ | $C$ | $Ax^2$ | $Bx$ | $C$ |
| | −2.70E-08 | 9.29E-05 | 2.65E-01 | −7.51E-09 | 1.55E-05 | 2.07E-01 | −1.94E-08 | 5.04E-05 | 1.59E-01 | 1.18E-09 | −2.07E-05 | 1.77E-01 | 5.91E-10 | −2.08E-05 | 1.91E-01 |
| RMS | | 0.004 | | | 0.003 | | | 0.006 | | | 0.006 | | | 0.006 | |

| Spectrum | Syrtis Central Lavas—CPX | | | Syrtis Central Lavas—CPX/OPX/OL | | |
|---|---|---|---|---|---|---|
| Mineral | Center | Width | Strength | Center | Width | Strength |
| Olivine | | | | 882 | 157 | −0.04 |
| | | | | 1095 | 173 | −0.08 |
| | | | | 1217 | 351 | −0.05 |
| LCP | | | | 897 | 125 | −0.05 |
| | | | | - | - | - |
| | | | | 1900 | 541 | −0.04 |
| HCP | 986 | 332 | −0.12 | 991 | 118 | −0.06 |
| | 1215 | 296 | −0.04 | - | - | - |
| | 2107 | 591 | −0.08 | 2226 | 566 | −0.08 |
| Continuum | $Ax^2$ | $Bx$ | $C$ | $Ax^2$ | $Bx$ | $C$ |
| | 5.06E-09 | −3.65E-05 | 1.63E-01 | 2.76E-09 | −2.67E-05 | 1.55E-01 |
| RMS | 0.006 | 0.004 | | | | |

[a]The absorptions centers, widths, and strengths as defined for each modified Gaussian related to the mafic mineralogy used in the validated configuration are reported. Additional Gaussians, dedicated to the UV absorption and to ferric/hydration/alteration effects (see section 3), are not reported here as they are not of interest considering mafic mineralogies (but they appear in Figure 5). Estimation of the fit quality over the whole spectral range (RMS) is also indicated. The MGM results for the spectra associated with the north crust, south crust, peripheral lavas, Nili Patera and Nili Fossae and the MGM results for the central lavas spectrum are given. It shows that the ternary configuration (CPX/OPX/OL) yields better fits than the CPX alone configuration in terms of spectroscopic constraints (see for instance HCP widths in the 1 and 2 μm regions).

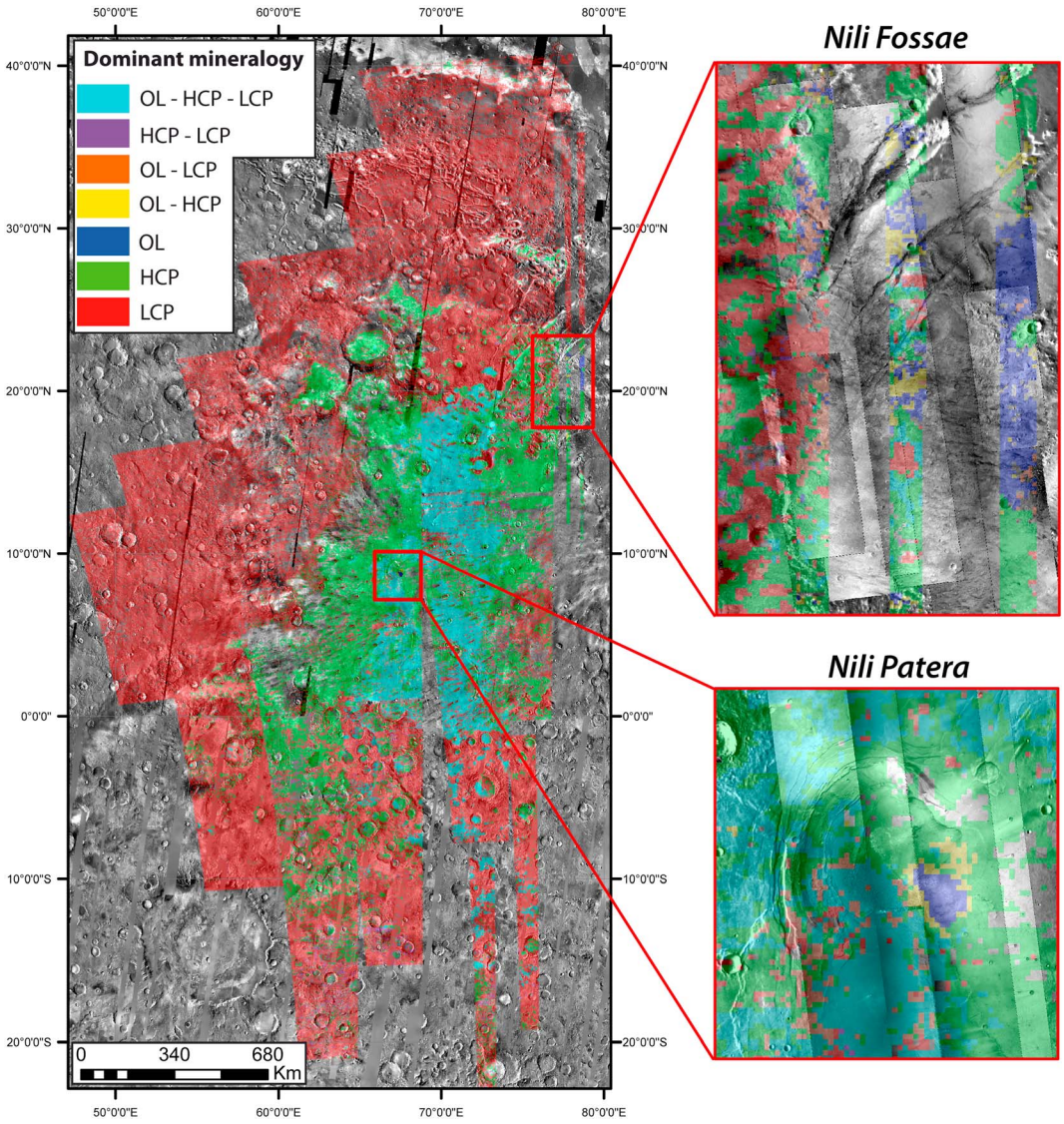


**Figure 6.** Dominant mineralogy for each pixel as in Figure 2 over a global THEMIS daytime thermal infrared mosaic. Three main units are found. Two of them are monopyroxene dominated with red pixels corresponding to Noachian crust and green pixels corresponding to Syrtis Major peripheral lavas. The last unit (cyan pixels) is located in the central part of the volcanic edifice and is detected as a ternary mixture involving both olivine and two pyroxenes. Two areas, Nili Patera and Nili Fossae, show a very strong enrichment in olivine. OMEGA mosaic has been created using the following hyperspectral images: ORB0576_3, ORB0576_4, ORB0554_4, ORB0554_3, ORB0521_4, ORB0521_3, ORB0521_2, ORB0422_5, ORB0422_4, ORB0422_3, ORB0422_2, ORB0444_4, ORB0444_3, ORB0444_2, ORB0444_1, ORB0488_2, ORB0488_3, ORB0488_4, ORB0988_5, ORB0966_5, ORB0955_5. On the two zoomed areas on the right side, Mars Reconnaissance Orbiter (MRO) Context Camera (CTX) images (P12_005789_2028, P21_009151_2014, P03_002321_2013, P15_006857_1993, G17_024948_2000, B02_010496_2005, P05_002888_2025, B06_011841_2005, P13_006211_2038, P15_006712_2010, P15_006778_2002, B11_013964_2038, P17_007780_1987, P21_009191_1895, P17_007609_1883, P05_003139_1887, P16_007398_1893, P08_004339_1888) are also used as background images (ISIS3 calibration).

HCP and minor amounts of LCP, with feldspar and more or less olivine [*Mustard et al*., 1997, 2005; *Poulet et al*., 2003; *Combe et al*., 2008]. *Reyes and Christensen* [1994] have proposed that such compositions could be similar to komatiitic basalts (i.e., basalts derived from a komatiitic melt by high degree of fractional crystallization). Such an association between komatiites and komatiitic basalts is documented on Earth in Archean terranes and bears witness to high mantle temperatures in the young Earth (~300°C higher than today). More recent estimates given by *Poulet et al*. [2009] are of 34 ± 7% HCP, 9 ± 3% LCP, 48 ± 9% neutral component (i.e., plagioclase or Si-rich phases), and less than 5% olivine. *Bandfield et al*. [2000] and *Hamilton et al*. [2001], using Thermal Emission Spectrometer (TES) onboard Mars

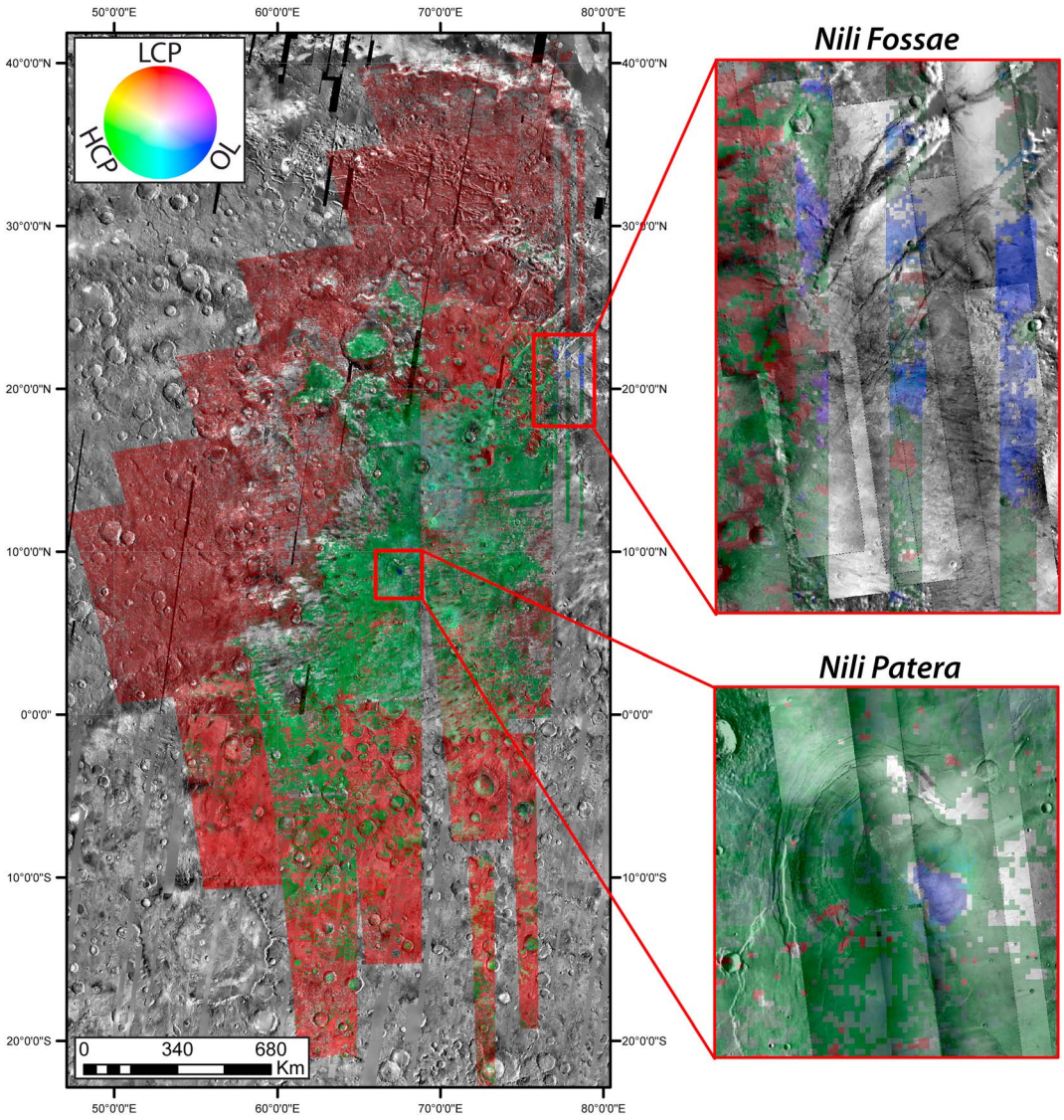


**Figure 7.** RGB composite map based on the relative band strengths derived from the MGM deconvolution of the three mafic minerals (red: orthopyroxene 1 µm Gaussian; green: clinopyroxene 1 µm Gaussian; blue: olivine 1.25 µm Gaussian) over a daytime thermal infrared mosaic. With such a representation, HCP appears as the dominant mineral in the mixture across Syrtis Major lavas in agreement with previous work [e.g., *Combe et al*., 2008; *Mustard et al*., 2005]. On the two zooms on the right side, MRO/CTX images are also used as background images. This case shows that RGB representation may be somehow misleading as it tends to oversimplify the rendition of the dominant mineralogy variation and distribution as revealed in Figure 6.

Global Surveyor (MGS), have found similar type of rocks (i.e., basaltic composition called "surface type 1"). *Rogers and Christensen* [2007] identified plagioclase (31%), HCP (29%) and LCP (4%), olivine (7%), and high-Si glass (12%).

[28] The regional surrounding crust shows an enrichment in LCP [e.g., *Combe et al*., 2008; *Mustard et al*., 2005; *Poulet et al*., 2007], while two areas in the vicinity of Syrtis Major show local enrichments in olivine: Nili Patera caldera and Nili Fossae region [e.g., *Combe et al*., 2008; *Hamilton and Christensen*, 2005; *Koeppen and Hamilton*, 2008; *Mustard et al*., 2005; *Poulet et al*., 2007]. Grain size has a strong effect on olivine spectra [*Poulet et al*., 2007; *Clenet et al*., 2011; *Ody et al*., 2013]. Accordingly, olivine composition in the Syrtis Major region has been interpreted to be either close to fayalite or forsterite-like but with large grain size [*Mustard et al*., 2007; *Poulet et al*., 2007; *Combe et al*., 2008; *Ody et al*., 2012]. Nili Patera caldera also exposes silica deposits produced by a volcanically driven hydrothermal system [*Skok et al*., 2010b]. The Nili Fossae region is of particular importance when considering the Noachian-Hesperian transition. Thus, some recent studies have focused on the local stratigraphy, particularly on alteration products [e.g., *Ehlmann et al*., 2009; *Mustard et al*., 2009; *Ehlmann and Mustard*, 2012; *Viviano and Moersch*, 2012].

### 5.1. OMEGA

[29] The OMEGA (Observatoire pour la Minéralogie, l'Eau, les Glaces et l'Activité) instrument onboard Mars

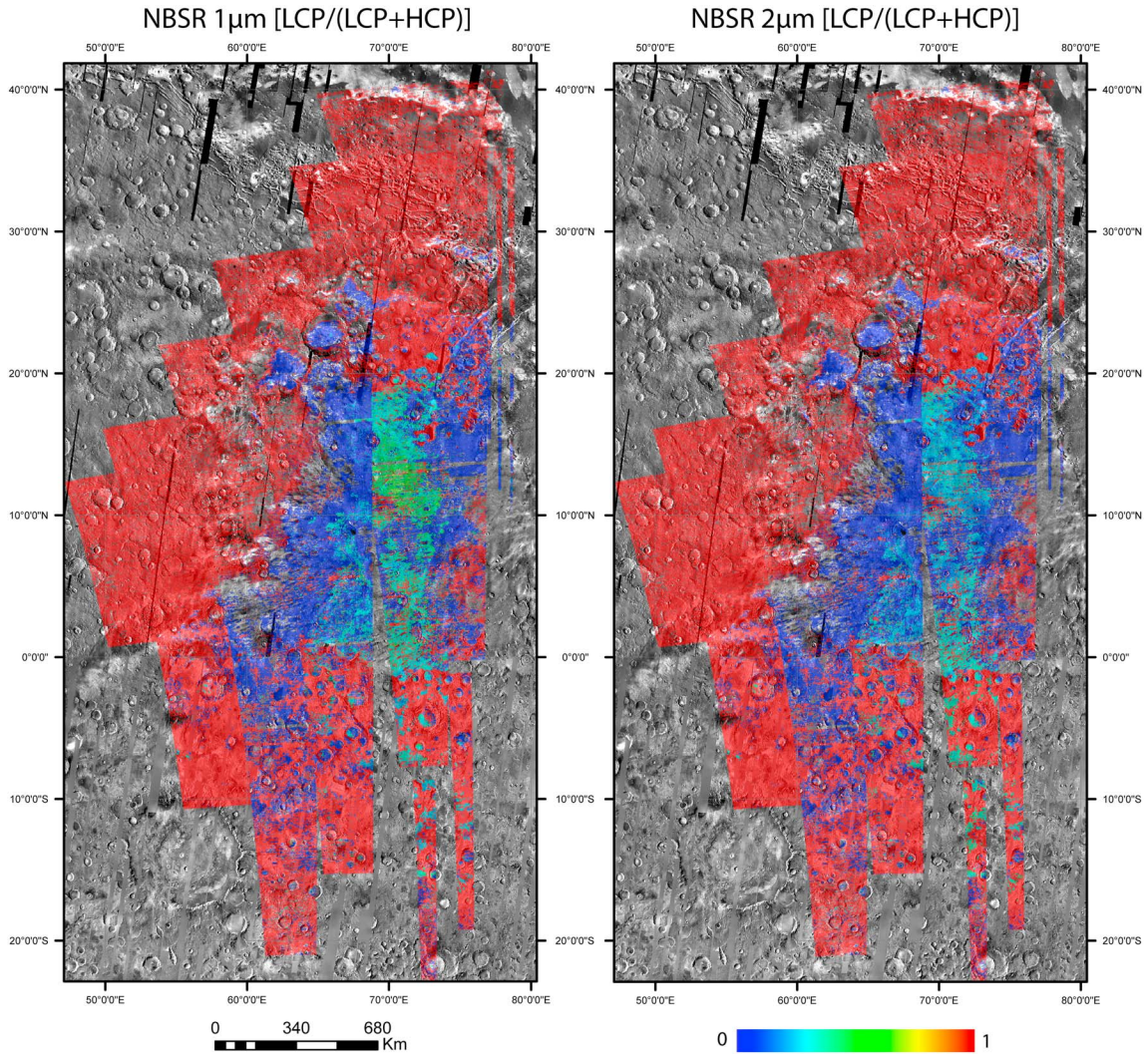


**Figure 8.** Normalized Band Strength Ratio (NBSR) between the strength of the LCP and HCP Gaussian parameters [LCP/(LCP + HCP)]. Left side corresponds to NBSR in the 1 µm wavelength domain while the right side corresponds to the 2 µm wavelength domain. Relative abundances of the two pyroxenes estimated from the MGM results (including ternary mixtures) are similar using independently the two absorption features. In general, HCP dominates in the Syrtis Major lavas although LCP appears to prevail in some spots in the central part of the edifice based on the 1 µm absorption-based NBSR estimate. See Figure 9 and text in section 5.3 for explanation.

Express [*Bibring et al*., 2004] operates from visible to thermal infrared (0.35–5.1 µm) using three detectors. In this work, only the VNIR and SWIR channels are used (0.35–2.73 µm). Spectral resolutions of the two detectors are respectively 7 and 13 nm. The field of view varies between 1.1° and 8.8° as a function of the spacecraft altitude, which implies a spatial resolution at global scale between 350 and 4800 m/pixel.

[30] Mosaic used in this work has been created using 21 hyperspectral images acquired in 2004 (details in Figure 6 caption). Each of them has been first instrumentally calibrated [*Bonello et al*., 2005; *Bellucci et al*., 2006]. The VNIR and SWIR channels are then radiometrically and spatially coregistered [*Carrozzo et al*., 2012], and an atmospheric correction is applied following the method in *Langevin et al*. [2005].

[31] Finally, we remove a few channels at the edge of the detectors as they show a lower signal-to-noise ratio. The final product is a hyperspectral mosaic ranging from 47.0°E to 78.8°E and 23.9°S to 41.5°N, with a spatial resolution of 32 pixels/degree, including both the Syrtis Major volcano, the Nili Fossae region, and the surrounding Noachian crust [*Greeley and Guest*, 1987]. The available spectral interval spanning the 0.49–2.60 µm domain is particularly suited for the detailed characterization of mafic assemblages and mixtures [*Burns*, 1993].

### 5.2. Regional Mapping Across Syrtis Major and Surroundings

[32] Spectra representative of the various regional lithological units have been extracted. Based on previous work [e.g., *Clenet et al*., 2008; *Pinet et al*., 2007], distinction can be made between the Noachian crust, the Syrtis Major lavas, and the two particular areas, Nili Patera and Nili Fossae. To test carefully for subtle spectroscopic variations within larger

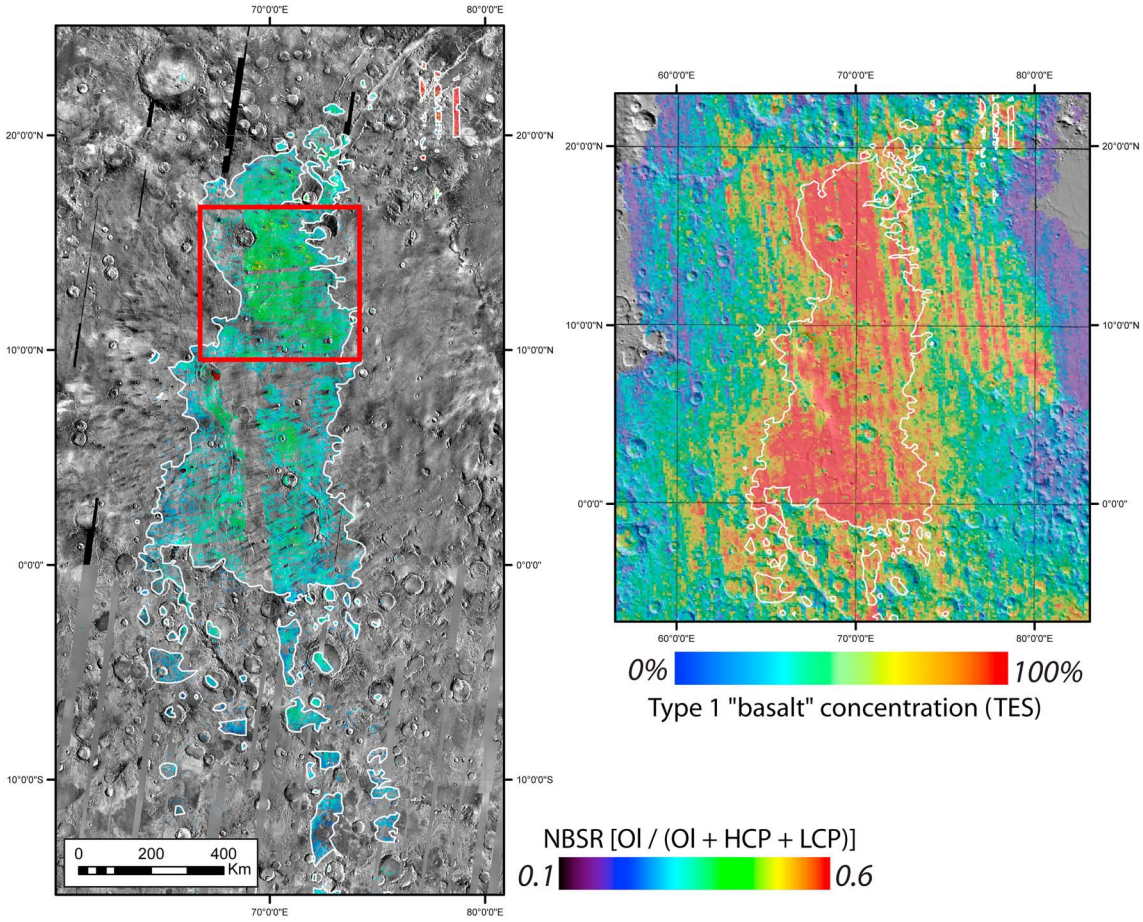


**Figure 9.** (left) NBSR between the strength of the olivine 1.25 µm Gaussian, the HCP 1 µm Gaussian, and the LCP 1 µm Gaussian when considering the olivine-clinopyroxene-orthopyroxene mixture configuration [OL/(OL + LCP + HCP)]. White line emphasizes the limit between the lithological units where olivine is found (central lavas and Nili Fossae) and the others where olivine is totally absent. Red box localize area shown in Figure 11. Nili Fossae and Nili Patera show the strongest enrichment in olivine (values > 0.6). (right) Comparison between our detection of olivine (white line, same as in the left subset) and the detection of "surface type 1" from *Bandfield et al.* [2000]. Red indicates a higher abundance of this particular unit in thermal infrared. A direct spatial correlation can be established between the two data sets.

units, two spectra are extracted from the crust (i.e., in the northern and in the southern crusts, outside Syrtis volcanic terrains) and from the volcanic lavas (i.e., central lavas and peripheral lavas). The localization of the six spectra on the mosaic is shown in Figure 4a and the spectra are displayed in Figure 4b. MGM has been run with the seven configurations on each of them, after applying a seven-spectel sliding window smoothing along the spectrum (Figure 4c). Sorting within the different mathematical solutions is done as in *Clenet et al.* [2011] and the final results are given in Figure 5 and the associated Table 1. All the solutions retained have a physical meaning consistent with previous results: The preexisting crust is found to be enriched in LCP (even if locally the crust could be partially altered and if in the northern area pyroxene signatures are partially masked by dust and/or ferric oxides [*Ody et al.*, 2012]), the Syrtis Major lavas are enriched in HCP, and the Nili Patera and Nili Fossae units are enriched in olivine. However, quite interestingly, two possible solutions are found for the central lava spectrum, the best mathematical solution being obtained using a ternary mixture configuration.

[33] This shows that composition variations exist within the volcanic edifice and that olivine may be also present in the central part of the edifice. Variations also exist within the crust as northern and southern areas do not have identical band centers. The next step is to expand these local results by means of a systematic mapping of the spectroscopic variability across the whole mosaic.

[34] As described previously for HyMap, the first step in MGM data processing on the whole data set consists of removing all the pixels with the more featureless spectra. The lowest values (1 µm absorption depth below 0.04) are found in the crust around the volcanic shield. In principle, those weak absorptions would not give reliable mathematical solutions in the case of complex mixtures [see *Clenet et al.*, 2011]. However, MGM analyses show that the only validated configuration in this area is a single pyroxene (Figures 5 and 6). As only one Gaussian function is needed for each wavelength domain at 1 and 2 µm, obtained

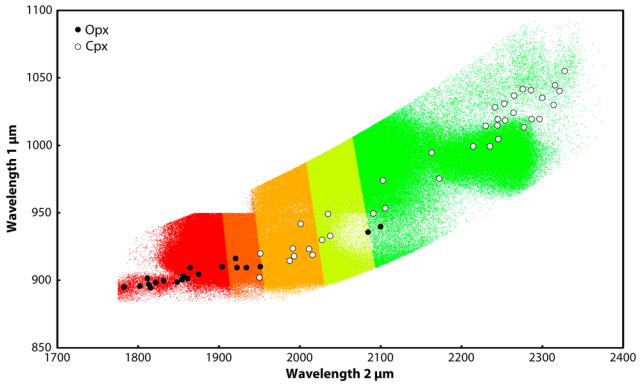


**Figure 10.** The dominant pyroxene phase present in each pixel of the mosaic is highlighted, on the basis of the spectroscopic variability seen in the 1 and 2 µm regions. Band centers are overplotted in the graph from *Adams* [1974]. The data (1 pixel in Figure 11 = 1 colored dot) are represented with a color coding spanning the whole range of spectral variations as evidenced in *Adams* [1974]. Color zone boundaries are defined arbitrarily, nonetheless, following the enstatite-ferrosilite-pigeonite-augite trend, to enhance the spectral variability (i.e., pyroxene compositional variation) spatially displayed in Figure 11.

parameters can be used to extract surface compositions there. High strengths of absorption features are found in the central and southern parts of the volcanic shield. The highest values are localized in the Nili Fossae area. Consequently, this assessment establishes that absorption features are strong enough on the volcano to be analyzed using MGM.

[35] Once this first test is performed, the MGM is then automatically initialized and run seven times with the different configurations on the whole data set, each pixel being handled independently. Seven mathematical solutions are obtained for each pixel. As described in section 4.2, the global fit quality is checked for each mosaic using RMS prior to any mineralogical analysis. Very few pixels are removed in the case of the OMEGA data set as only less than 1% of the whole mosaic does not verify the rejection threshold. Most of them are localized in the southern part of the mosaic, on the old highlands adjacent to the volcanic shield.

[36] The seven mathematical solutions are each tested to make sure that Gaussian functions parameters have a physical meaning (see section 3) [*Clenet et al*., 2011]. The final output results in a global mapping represented in Figure 6. As expected from individual spectrum analyses (Figure 5), only one configuration per pixel is kept both in the west to north crust (orthopyroxene configuration) and in the peripheral lavas of Syrtis Major (clinopyroxene configuration). In the central lavas unit, both clinopyroxene only and olivine-clinopyroxene-orthopyroxene configurations give reliable mathematical solutions as demonstrated in Table 1. The relative abundance of olivine, HCP, and LCP will be discussed using band strengths in the next section of the paper.

[37] For specific pixels, both an initialization dedicated to orthopyroxene alone and an initialization dedicated to clinopyroxene alone give realistic mathematical solutions. Our mathematical solutions (which are set free [see *Clenet et al*., 2011]) for each monopyroxene configuration converge toward an almost identical result, the band centers position varying within a few nanometers (see Table 1) which is within MGM uncertainties [*Kanner et al*., 2007]. Two different configurations are here validated because of the overlapping fields in pyroxenes band centers (i.e., pyroxenes can have intermediate compositions between LCP and HCP, with band centers satisfying both orthopyroxene and clinopyroxene trends as defined in *Adams* [1974]). Consequently, our MGM results are here indicative of the occurrence of an intermediate low-calcium pyroxene composition and accordingly, the choice is made to chart those pixels in red in Figure 6. Localization of those pixels is limited to cratered terrains south of the volcanic edifice (i.e., Noachian crust), in the southern part of the mosaic.

[38] Two small areas show an olivine-dominant mineralogy. First one is a little patch south-east of Nili Patera where only the olivine configuration is validated (bottom zoom in Figure 6). Interestingly, a narrow ring where both olivine and olivine-clinopyroxene configurations are kept is found around the patch, transitioning toward the surrounding HCP-rich lavas. A similar behavior is observed in the second area localized in the Nili Fossae region (top zoom in Figure 6). In this location, next to the olivine-only configuration, both olivine/HCP and olivine/LCP mixtures are also found.

[39] While these results agree with the olivine-rich outcrops detections proposed in previous studies [e.g., *Hamilton and Christensen*, 2005; *Mustard et al*., 2005; *Poulet et al*., 2007; *Combe et al*., 2008; *Koeppen and Hamilton*, 2008; *Ody et al*., 2013], the present work highlights the occurrence of local binary and/or ternary mafic mixtures involving olivine, associated with subtle spatial variations.

### 5.3. Olivine and Clinopyroxene Abundances in the Central Lavas

[40] The detection of olivine present in the central part of Syrtis Major shield does not however change the overall picture proposed from previous studies. At first order and as found in earlier works, pyroxene generally prevails in Syrtis Major lavas and, in this respect, our RGB map displayed in Figure 7 compares well with the HCP/LCP map from *Mustard et al*. [2007] or *Combe et al*. [2008]. Conversely, as expected, Nili Patera and Nili Fossae areas exhibit strong olivine absorptions even when dealing with olivine-pyroxene mixtures.

[41] A Normalized Band Strength Ratio (NBSR) [*Kanner et al*., 2007] based on MGM results can be used to estimate the relative proportion of each pyroxene in the different lithological units. Independent mapping at both 1 and 2 µm is represented in Figure 8. It is worth noticing that results are generally quite consistent using independently the two absorption domains. The map can be divided into three units, with the surrounding crust appearing as LCP-rich rocks while Syrtis peripheral lavas are enriched in HCP. In the central lavas, where our mapping approach detects an olivine-pyroxenes mixture, the NBSR estimate appears intermediate. While the 2 µm absorption-based NBSR estimate still indicates HCP as the dominant pyroxene, though to a lesser extent than that for the peripheral lavas, the 1 µm absorption-based NBSR estimate taken at face value seems to favor LCP. Actually as demonstrated in the following section, this is an indirect consequence of the presence of olivine contributing to the 1 µm absorption feature, resulting in a decrease of the 1

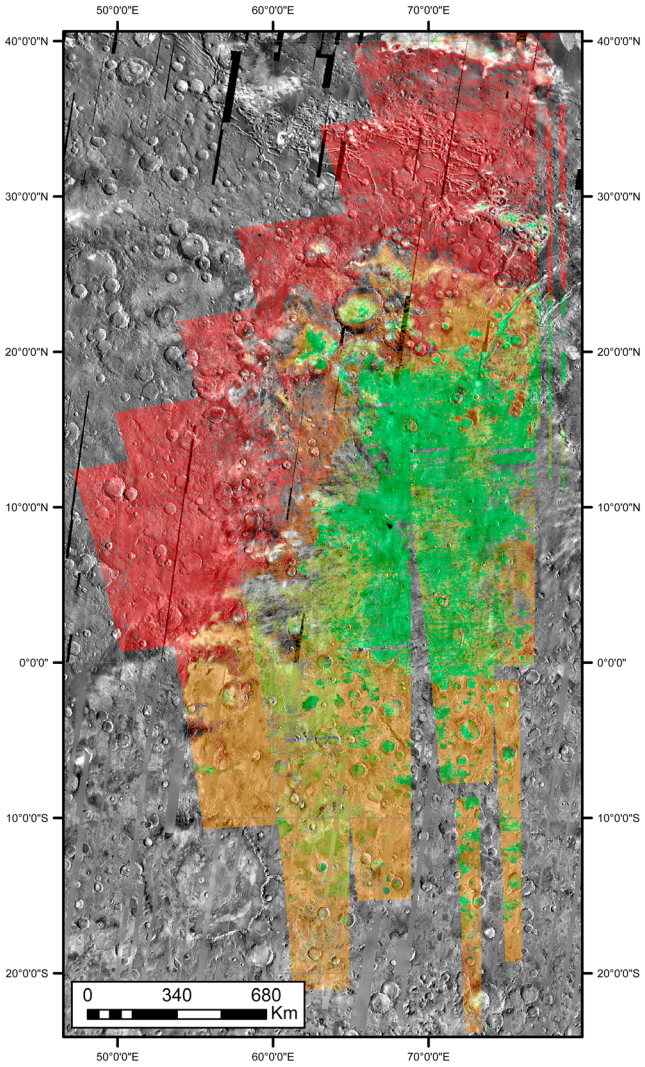


**Figure 11.** Map of pyroxenes compositions as determined by Adams' graph [*Adams*, 1974]. Color coding identical to Figure 10. As expected, the pyroxenes in the crust surrounding Syrtis Major show a lower calcium and iron content than the Syrtis lavas. We also observe two distinct compositions within the crust with the red area showing more enstatite-like pyroxenes while the crust south of the edifice is more pigeonite rich (orange area). We also observe two units in the volcanic edifice as low-Ca augite (yellow pixels) and high-Ca augite (green area). As such, there is a continuous compositional evolution between the crust and the subsequent lavas.

μm absorption band strength for HCP. In order to establish this as clearly as possible, we define a more general NBSR ratio, taking into account the olivine contribution, and extract the relative proportion of each mineral phase. Figure 9 shows the spatial distribution of the OL/(OL + HCP + LCP) ratio and indicates conspicuously that olivine is more abundant in the central part of the unit (i.e., a ratio of 0.4 or more); conversely, olivine becomes less and less abundant when approaching the peripheral lavas and is not found outside the unit boundary (white line in Figure 9). Nili Patera and Nili Fossae are the only areas where the olivine is dominating the signal (i.e., 0.6 or more). Due to the lack of laboratory series of spectra with systematic variations in relative abundances, olivine-orthopyroxene-clinopyroxene mixtures have not been studied as much as olivine-orthopyroxene mixtures and, as it stands, for the time being, one cannot go beyond relative proportions for the three mafic abundances.

### 5.4. Chemical Compositions

[42] The approach implemented in the present work is a significant step forward to characterize not only the modal but also the chemical compositional variations of pyroxenes and olivines. As explained in *Sunshine et al*. [1990], the band center positions associated with the different mafic minerals are not predetermined in the inverse problem and the MGM outputs are thus truly informative of the chemical composition of pyroxenes and olivines.

[43] Chemical composition of olivines is determined on the basis of the position of the three absorption centers as explained in *Sunshine and Pieters* [1998] and *Clenet et al.* [2011]. When considering the pixels for which only the mineral olivine is found (i.e., Nili Patera and Nili Fossae regions), retrieved compositions range mainly from $Fo_{50}$ to $Fo_{80}$. These results are consistent with TES observations [*Hoefen et al*., 2003; *Koeppen and Hamilton*, 2008]. Locally, band centers are shifted to longer wavelength which could indicate $Fo_{25\text{-}40}$ compositions or larger grain size [*Poulet et al*., 2007; *Clenet et al*., 2011; *Ody et al*., 2013]. From laboratory work, uncertainties on the composition due to the method in this range of iron content are on the order of ±10% [*Clenet*, 2009]. When looking at the olivine iron content in the case of the olivine-pyroxenes mixtures (i.e., in the Syrtis Major lavas), the whole range of composition is covered. Such diversity could be explained by grain size and/or mixture effects. Nevertheless, most of the pixels are still associated with a composition between $Fo_{50}$ and $Fo_{80}$, consistent with what we have found in olivine-rich areas.

[44] The detection of pyroxene in a given pixel of the mosaic may result from a monopyroxene configuration or from a binary/ternary configuration. To address the matter of pyroxene compositional variations across Syrtis Major shield and surroundings, the choice is made to document the dominant pyroxene phase in each pixel of the mosaic. The spectroscopic variability seen in the 1 and 2 μm domain is then documented in Figure 10, displaying the band center position in both spectral domains as an overplot in *Adams*' [1974] graph. The data are represented with a color coding spanning the whole range of spectral variations as evidenced in *Adams* [1974].

[45] The first type of pyroxene found is the one associated to the northern Noachian crust (red dots and pixels in Figures 10 and 11, respectively). The positions of the absorption centers at 1 and 2 μm range from about 890 to 950 nm and 1800 to 1910 nm, respectively. Based on *Cloutis and Gaffey* [1991a], this indicates enstatite-like orthopyroxenes, with relatively low iron and very low calcium content. This kind of composition is also found for the nondominant low-calcium pyroxene phase in the case of the ternary mixture characterizing the central lavas of the shield (see Table 1).

[46] A strength of the MGM approach is to be able to distinguish pyroxenes with intermediate composition from mixtures of two distinct pyroxenes [*Sunshine and Pieters*, 1993], even when considering mixtures also involving

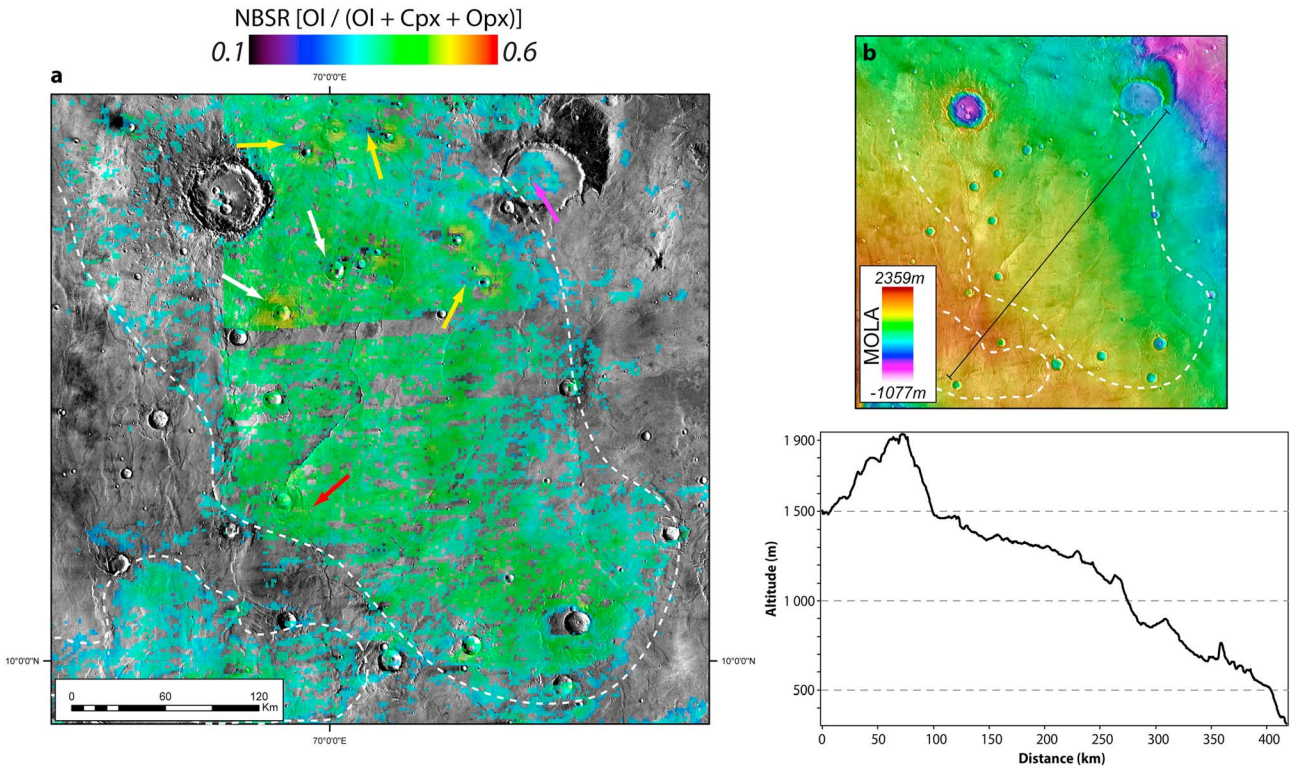


**Figure 12.** (a) NBSR between olivine and clinopyroxene strengths, as described in Figure 9, over a daytime thermal infrared mosaic. Represented area is localized on the volcanic edifice by the red box in Figure 9. White dashed lines outline olivine-rich zones. (b) MOLA elevation over the same area as inset a. The slope is globally oriented SW-NE as represented on the profile. Arrows indicate locations of particular interest to test the relationship between morphologies and olivine detections. Red and white arrows are related to impact craters, while yellow arrows indicate morphologies related to wind. See section 5.5.1 for interpretation.

olivine [*Clenet et al*., 2011]. In the southern crust and at the boundary between the volcanic edifice and the northern crust, band center positions are slightly at longer wavelength than those for previous orthopyroxene. Hence, our MGM approach reveals a second type of LCP (orange dots and pixels in Figures 10 and 11, respectively). Transition between the two crust compositions appears to be well defined. Data from *Cloutis and Gaffey* [1991a] suggest an intermediate pyroxene, either an orthopyroxene with more iron in the structure than for the previous unit or a low-iron, low-calcium clinopyroxene (i.e., pigeonite).

[47] Then a whole range of calcium-rich pyroxenes is found, with absorption centers showing a large variability. Position in the 1 µm domain evolves between 920 and 1050 nm while centers in the 2 µm wavelength domain are between 2025 and 2300 nm. We nevertheless distinguish between two groups (dots and pixels colored in yellow and green in Figures 10 and 11, respectively). The ones with the lowest absorption centers are located mainly at the boundary between lavas and Noachian crust while the pixels with the highest absorption centers are globally located in the central part of the volcanic structure. Absorption center values found span the whole composition range, at least in terms of calcium content, between low-Ca and high-Ca augite. Interestingly, this approach shows that no evidence of diopside is found. The geological implications of these results are addressed in the following section.

## 5.5. Discussion

### 5.5.1. Lithology Versus Morphology

[48] Our study agrees with the previous ones in terms of global mineralogical trends, with the detection of HCP enrichment of the volcanic edifice compared to the surrounding Noachian crust, and the presence of olivine in Nili Patera and Nili Fossae. The aim here is not to discuss the geological interpretation of such particular units as it has already been intensively debated [e.g., *Christensen et al*., 2005; *Mustard et al*., 2007; *Poulet et al*., 2009; *Skok et al*., 2010a] but to focus on the central lavas unit which shows a composition that is richer in olivine than previously thought.

[49] It has been proposed that the olivine enrichment in the Syrtis Major region is only related to the presence of sand dunes fields or to the dust coverage [e.g., *Christensen et al*., 2005; *Poulet et al*., 2009]. Sand sources would then be the nearby olivine-rich rocky outcrops observed in Nili Patera and Nili Fossae. In such a hypothesis, wind drives the erosion and deposition processes. Studies of Earth analogs show that sorting of minerals according to their density and grain size can occur in similar environments [*Mangold et al*., 2011]. This process may change the apparent modal composition of igneous outcrops through the formation of "placers" enriched in a specific mineral species or by settling of thick dust coverage.

[50] However, the relationship between olivine amounts detected with our adapted MGM approach and morphological features is not so simple and is not consistent with eolian

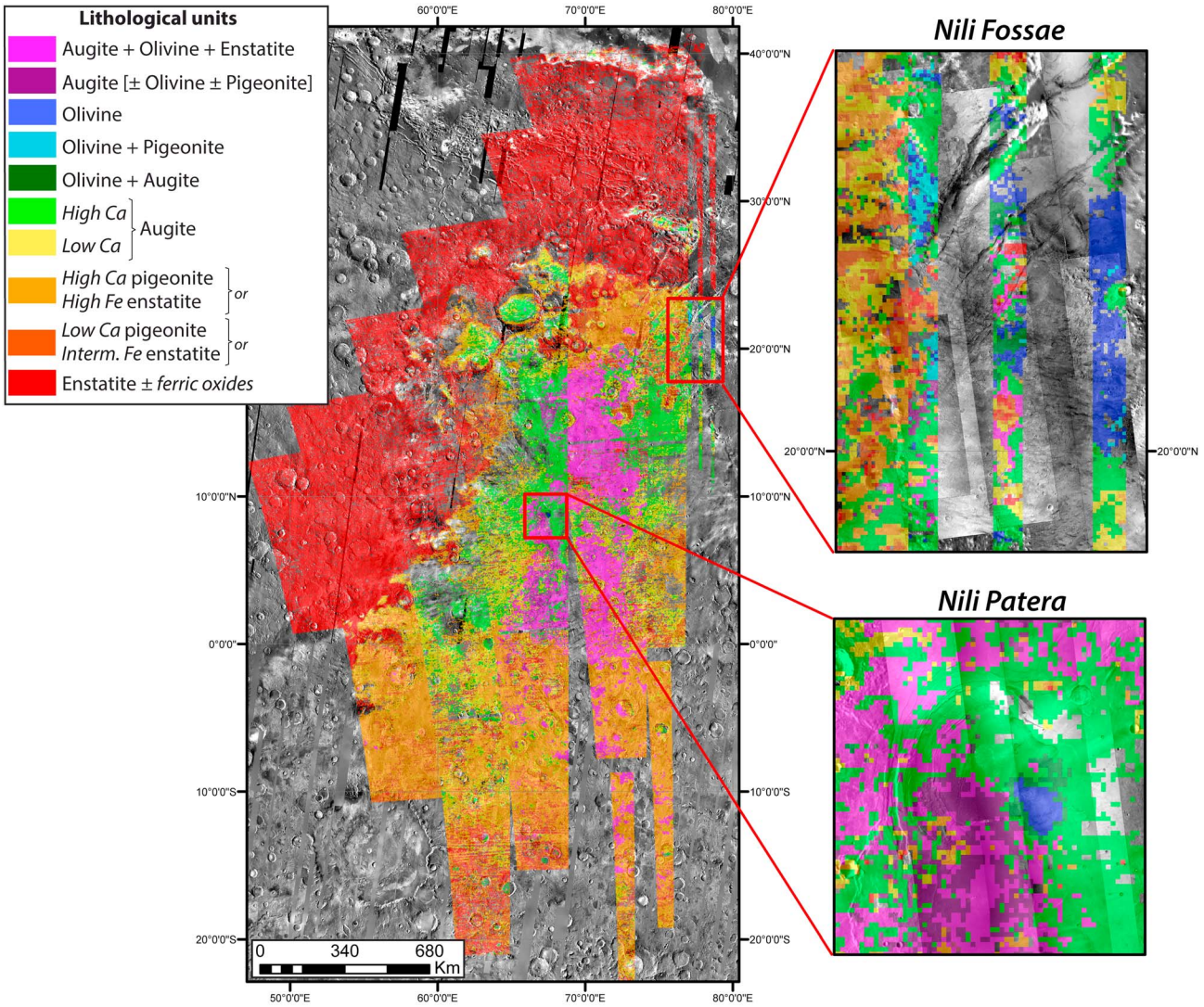


**Figure 13.** Lithological map of the Syrtis Major area based on a synthesis of the dominant mineralogy and the chemical composition. Five main units can be distinguished: the northern crust and the southern crust, which have a different composition, the peripheral and central lavas which show an enrichment in olivine, and finally Nili Patera and Nili Fossae which are dominated by olivine-rich rocks.

control of the mineralogy, at least at OMEGA scale. Lavas compositions are not homogeneous and several locations show a local enrichment in olivine, as highlighted in Figure 12 with the white dashed lines. Using Mars Orbiter Laser Altimeter (MOLA) elevation data set, one can show that the variations are unrelated to the regional topography. Indeed, the slope is globally oriented SW-NE in the zoomed area and no obvious correlation exists with olivine detections. Similar abundances are found at both higher and lower altitudes and on both the northern and eastern flanks of the volcano. Thereby, this observation points rather toward local compositional variations of igneous origin.

[51] At a local scale, wind plays an important role in moving fine dust particles. Figure 12 shows that two situations can occur regarding this effect. The pink arrow points toward a large crater where the floor has been covered by sand or dust. This is evidenced by the particularly smooth aspect observed on high-resolution visible imagery and it is pretty clear from our mapping that such deposits cover only a limited part of the crater floor and that the rims exhibit different compositions.

[52] Yellow arrows point at some locations where bright wind streaks can be observed on high-resolution visible images. Those wind streaks are all located next to impact craters with their respective orientations directly correlated to regional wind direction (i.e., globally E-W). In our mapping, they appear to be depleted in olivine compared to surrounding terrains (bluish in Figure 12). Assuming that the Martian dust is enriched in pyroxene, a dust-component increase would result in a partial masking of olivine signatures. Consequently, wind effect would tend to decrease the apparent content of olivine instead of increasing it as expected from grain segregation. This implies that detections of higher olivine content are here unrelated to eolian morphologies and rather indicative of compositional variations in the bedrock.

[53] The second effect which could modify the contribution of each mafic mineral is related to impact processes.

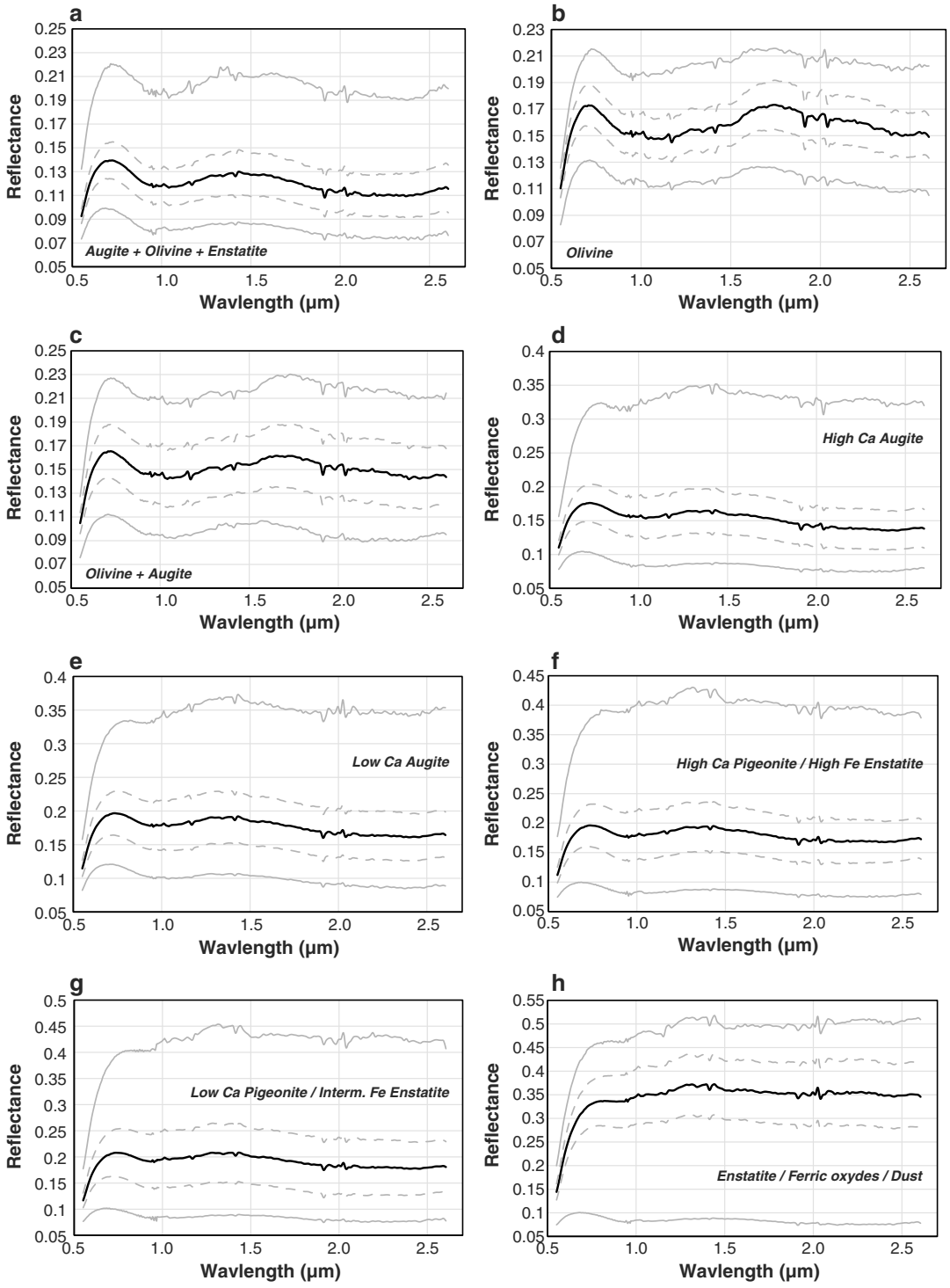


**Figure 14.** Statistics on spectra extracted from the most representative lithological units displayed in Figure 13. Reported on each graph, from top to bottom, are the maximum, the positive standard deviation, the mean, the negative standard deviation, and the minimum spectrum for each unit. (a) The augite + olivine + enstatite unit (i.e., central lavas), (b) the olivine-rich units (includes both Nili Patera and Nili Fossae regions), (c) the olivine + augite unit, (d) the high-Ca augite unit (i.e., peripheral lavas), (e) the low-Ca augite unit (i.e., peripheral lavas), (f) the high-Ca pigeonite or high-Fe enstatite unit (i.e., southern crust), (g) the low-Ca pigeonite or intermediate Fe-enstatite unit (i.e., boundary between Syrtis lavas and northern crust), and (h) the enstatite ± ferric oxides ± dust unit (i.e., northern crust).

**Table 2.** Parameters Obtained Using Our MGM Procedure on the Eight Mean Spectra From the Most Representative Lithological Units Found in Figure 13[a]

| Spectrum | Augite + Olivine + Enstatite | | | Olivine | | | Olivine + Augite | | | High-Ca Augite | | |
|---|---|---|---|---|---|---|---|---|---|---|---|---|
| No. Pixels | 86,369 | | | 868 | | | 380 | | | 81,885 | | |
| Mineral | Center | Width | Strength | Center | Width | Strength | Center | Width | Strength | Center | Width | Strength |
| Olivine | 877 | 140.00 | −0.07 | 878 | 175.00 | −0.08 | 882 | 145 | −0.07 | | | |
| | 1094 | 169.00 | −0.09 | 1056 | 274.00 | −0.06 | 1104 | 188 | −0.06 | | | |
| | 1219 | 351.00 | −0.07 | 1222 | 507.00 | −0.14 | 1307 | 472 | −0.11 | | | |
| LCP | 918 | 125 | −0.05 | | | | | | | | | |
| | - | - | - | | | | | | | | | |
| | 1858 | 556 | −0.07 | | | | | | | | | |
| HCP | 992 | 133.00 | −0.07 | 992 | 229.00 | −0.07 | 999 | 315.00 | −0.10 | | | |
| | - | - | - | - | - | - | 1198 | 299.00 | −0.01 | | | |
| | 2239 | 549.00 | −0.10 | 2133 | 562.00 | −0.06 | 2109 | 579.00 | −0.07 | | | |
| Continuum | $Ax^2$ | $Bx$ | $C$ | $Ax^2$ | $Bx$ | $C$ | $Ax^2$ | $Bx$ | $C$ | $Ax^2$ | $Bx$ | $C$ |
| | −2.30E-09 | −2.30E-06 | 1.41E-01 | −1.22E-08 | 2.66E-05 | 1.62E-01 | −1.17E-08 | 2.88E-05 | 1.50E-01 | 4.81E-10 | −2.10E-05 | 1.92E-01 |
| RMS | | 0.008 | | | 0.010 | | | 0.009 | | | 0.009 | |

| Spectrum | Low-Ca Augite | | | High-Ca Pigeonite/High-Fe Enstatite | | | Low-Ca Pigeonite/Intermediate-Fe Enstatite | | | Enstatite/Ferric Oxide/Dust | | |
|---|---|---|---|---|---|---|---|---|---|---|---|---|
| No. Pixels | 118,115 | | | 207,334 | | | 76,156 | | | 346,207 | | |
| Mineral | Center | Width | Strength | Center | Width | Strength | Center | Width | Strength | Center | Width | Strength |
| Olivine | | | | | | | | | | | | |
| LCP | | 919 | 157 | −0.07 | 914 | 140 | −0.06 | 908 | 146 | −0.03 | | |
| | | 1086 | 274 | −0.07 | 1084 | 275 | −0.06 | 1102 | 289 | −0.02 | | |
| | | 1989 | 634 | −0.11 | 1971 | 642 | −0.11 | 1878 | 629 | −0.08 | | |
| HCP | 984 | 284.00 | −0.09 | | | | | | | | | |
| | 1196 | 299.00 | −0.01 | | | | | | | | | |
| | 2065 | 599.00 | −0.07 | | | | | | | | | |
| Continuum | $Ax^2$ | $Bx$ | $C$ | $Ax^2$ | $Bx$ | $C$ | $Ax^2$ | $Bx$ | $C$ | $Ax^2$ | $Bx$ | $C$ |
| | −3.58E-09 | −4.20E-06 | 2.01E-01 | −9.31E-09 | 2.03E-05 | 1.85E-01 | −1.37E-08 | 3.31E-05 | 1.89E-01 | −4.29E-08 | 1.50E-04 | 2.48E-01 |
| RMS | | 0.010 | | | 0.008 | | | 0.008 | | | 0.007 | |

[a]The first line indicates the number of pixels that are included in each class. As in Table 1, the absorptions centers, widths, and strengths as defined for each modified Gaussian related to the mafic mineralogy used in the validated configuration are reported. Estimation of the fit quality over the whole spectral range (RMS) is also indicated. The MGM results for the spectra associated with the augite + olivine + enstatite unit (i.e., central lavas), olivine unit (including both Nili Patera and Nili Fossae regions), olivine + augite unit (next to the olivine unit in Nili Patera and Nili Fossae regions), and high-Ca augite unit (i.e., part of the peripheral lavas and the MGM results for the spectra associated with the low-Ca augite unit (i.e., other part of the peripheral lavas), high-Ca pigeonite or high-Fe enstatite unit (i.e., southern crust), and low-Ca pigeonite or intermediate Fe enstatite unit (i.e., boundary between Syrtis lavas and northern crust) and enstatite ± ferric oxides ± dust unit (i.e., northern crust) are given.

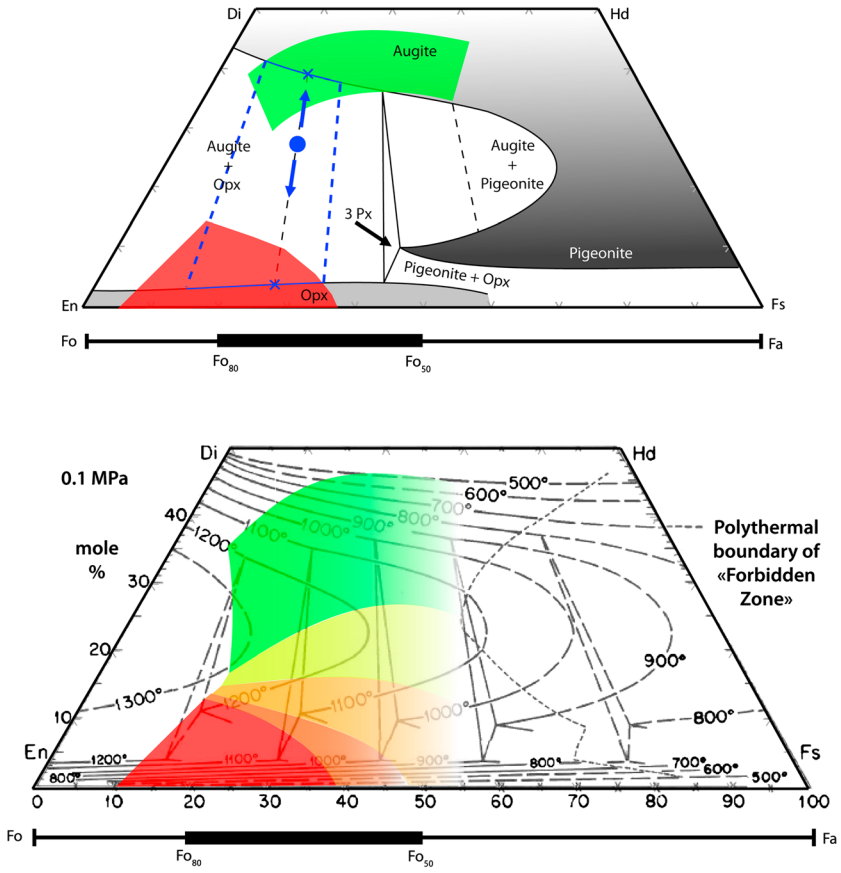


**Figure 15.** Pyroxenes thermometry using data from *Lindsley* [1983] and MGM results. The range of olivine compositions extracted from MGM in the Nili Fossae area are also reported below the quadrilateral. (top) The central lavas are a mixture with both augite and enstatite, which could be related to lavas erupted at lower temperature (below 1000°C). (bottom) Conversely, all the other units previously discussed, including Syrtis Major peripheral lavas, exhibit simple compositions covering a large part of the pyroxene chemical composition range. To crystallize outside the immiscibility gap implies higher temperatures (or higher pressure). Considering data at 1 atm, such composition implies temperature above 1250–1300°C.

*Baratoux et al*. [2005, 2007] have demonstrated that impact ejecta at Syrtis Major are controlled more by rock-size distributions inherited immediately after impact than by air-fall dust and mantling processes. In our mapping, two situations occur when considering impact processes. On the one hand, similar olivine amounts can be found within and outside the ejecta blanket of a unique crater (e.g., red arrow in Figure 12). This suggests that the observed olivine variations are not influenced by the fresh rocky blocks excavated during the impact but are rather driven by lava composition.

[54] On the other hand, two close craters with similar diameters (i.e., similar depth of excavation) can show different olivine abundances (e.g., white arrows in Figure 12). There are even examples of pairs of close craters with similar diameters having a similar continuous ejecta blanket but displaying different mineralogical signatures. *Baratoux et al.* [2007] have shown that craters with enrichment in HCP are spatially randomly distributed. As it stands, our observations suggest that the olivine abundance is not controlled by the impact process itself but rather depends on the subsurface structure of the volcanic edifice and possibly of its mode and time of emplacement. *Baratoux et al*. [2007], and later on *Skok et al*. [2010a], have suggested a temporal relationship for those craters. They have proposed that the enrichment in HCP represents the true composition of the Syrtis Major volcanics and that surfaces older than 2 Ga have been altered under different Hesperian conditions. We observe olivine enrichment only in the central part of the volcanic edifice (Figure 9) and the ejecta with the highest olivine concentration are localized around the same craters as the one referenced as spectrally distinct by *Baratoux et al*. [2007] and *Skok et al*. [2010a]. Thus, this does not change the interpretation of two distinct units within the Syrtis Major volcano, while in agreement with the proposed scenario of late alteration.

### 5.5.2. Mineralogic Mapping

[55] As detailed previously, several distinct lithological units are found in the studied area. All the information obtained from our systematic MGM approach results and described in previous sections can be synthesized to generate a more accurate mapping driven by mineralogy. The results are presented in Figure 13, using both modal abundance and chemical variations.

[56] Compared to previous work which produced similar maps to the one shown in Figure 7 [e.g., *Combe et al*.,

2008; *Mustard et al*., 2005], Figure 13 exhibits more complexity. The crust surrounding the Syrtis Major volcano is now subdivided in two areas. The northern part is enriched in enstatite-like orthopyroxenes, with more or less ferric oxides covering the outcrops. In the case of the southern crust, an ambiguity exists for the composition. Indeed, values for absorption band centers can be explained both with low- to high-Ca pigeonite and with low- to high-Fe enstatite [*Cloutis and Gaffey*, 1991a]. There is actually no way to clearly make the distinction based solely on laboratory work. Nevertheless, *Clenet et al*. [2012] and *Skok et al*. [2012] have carried out analyses on crustal pyroxenes on the southern highlands and their results are consistent with low-Ca, moderately Fe-rich pyroxene. In our case, this could indicate an evolution of the crustal composition in Syrtis Major region from the enstatite end-member ($Wo_0En_{100}Fe_0$) toward the hypersthene end-member ($Wo_0En_{50}Fe_{50}$).

[57] The volcanic edifice itself appears to include two units. The peripheral lavas (yellow and green in Figure 13) show a strong enrichment in high-Ca pyroxenes. Those pyroxenes have compositions in the range of augite (with various calcium contents) rather than diopside as initially proposed by *Poulet et al*. [2007]. Moreover, as the MGM approach from *Clenet et al*. [2011] is able to handle only spectral type B clinopyroxenes, those augites are more likely Mg rich rather than Fe rich. The central lavas of Syrtis characterized by a ternary mafic mixture present also an augitic composition, combined with enstatite and olivine. This central unit has not been defined previously but appears now to be different from the surrounding lavas. Finally, the two areas enriched in olivine (i.e., Nili Patera and Nili Fossae) are also mapped with some variations in the associated pyroxene content.

[58] It is of interest to look carefully at the central lavas unit distribution. In Figure 9, limits of our olivine detections have been outlined (left side of the figure) and compared to the detection of Type 1 "basalt" concentration as defined by *Bandfield* [2002] using thermal infrared (right side of the figure). It appears that the two detections agree well, even if the MGM-based detection is more intermittent in the southern part of the volcanic edifice and may be a consequence of residual imperfections in the mosaicking process. This correlation between visible near-infrared and thermal infrared is an additional independent observation in favor of actual lithological variations occurring in the central part of Syrtis Major.

[59] Finally, representative spectra have been extracted using all the pixels associated with the main units described above (the augite [±olivine ± pigeonite] and the olivine + pigeonite units have not been reported as they do not represent large spatial extent and their spectral behavior are similar respectively to the augite + olivine + enstatite and the olivine + augite units). The most extreme spectra, the standard deviation, and the average spectra are reported in Figure 14. It appears at first order that spectral variations between the different units are generally subtle, except for the particular units that are the olivine-rich regions and the northern crust. The maximum spectra for the Syrtis Major lavas and the southern crust (Figures 14d–14g) exhibit particular spectral shapes compared to the respective average spectra but they are not truly representative of the units as they are always far away from the standard deviation. MGM results for each average spectrum are reported in Table 2. The results are coherent with the expected literature trends [*Adams*, 1974; *Sunshine and Pieters*, 1993, 1998] and what has been found on the six test spectra (section 5.3). The distinction made within the peripheral lavas (high-Ca and low-Ca augite units) and within the Southern crust (high-Ca pigeonite/high-Fe enstatite and low-Ca pigeonite/intermediate-Fe enstatite) is confirmed to be subtle as each time very little changes are observed between the different band centers. This points toward a progressive evolution of the igneous processes rather than abrupt changes.

#### 5.5.3. Pyroxenes Thermometry and Local Geological History

[60] Based on pyroxenes compositions estimated from MGM results, one can then address first-order implications on the Martian thermal structure and evolution using experimental data from *Lindsley* [1983]. Indeed, with a similar parent melt composition, the nature and composition of the crystallizing pyroxenes vary according to temperature and pressure. Figure 15 shows the different compositions described in section 5.4 reported in two diagrams: The top corresponds to the central lavas unit while the bottom corresponds to the rest of the studied region.

[61] In the central unit, two types of pyroxenes are associated (augite and enstatite, respectively, green and red fields in Figure 15, top). Due to the pyroxenes immiscibility gap, the way to produce such a combination is to crystallize a magma of intermediate composition, in terms of calcium and iron content (e.g., blue dot), at low pressure (0.1 MPa) and temperature (below 1000°C). Based on our analysis, enstatite and augite compositions would be delimited by the blue dashed line in Figure 15 (top) with an iron content fitting pretty well the associated olivine chemical compositions ($Fo_{50\text{-}80}$). Conversely, to produce only one pyroxene at a time with an intermediate composition, as it is observed in the case of the peripheral lavas (yellow and green fields, Figure 15, bottom), higher crystallization temperatures are required (above 1250–1300°C), which implies more magnesian parent melts. As we observe both situations in the Syrtis Major area, it implies that the lavas temperature of crystallization is likely to have changed over time. The central lavas being representative of lower temperature conditions, the temperature path we observe would be directly correlated to the construction of the volcanic structure and the cooling of the magmatic chamber along eruption time.

[62] Accordingly, the scenario for the regional history could be as follows. The surrounding crust would have been produced at the Noachian time, as proposed by *Skok et al*. [2012]. Crystallization of a magma ocean starts with the Mg-richest olivine and pyroxenes, forming a cumulate pile at the bottom of the ocean. As crystallization progressed, the cumulus minerals were progressively enriched in Fe, and their density increased accordingly (the density of pyroxenes increases by about 25% from the pure Mg pole to the pure Fe pole). High-density minerals that settled at the top of the pile may become sufficiently unstable to trigger a global mantle overturn. The upwelling of Mg-rich rocks would counterbalance the sink of dense material. Decompression melting could be a consequence of such mass redistribution. Large volume of lavas could be produced in this way during a relatively short time span, a situation analog to the one that prevailed on Earth during the formation of large igneous provinces. The cooling would be slow enough to

make possible the formation of magma chambers that eventually crystallized into layered cumulate layers. Finally, pyroxenes exposed on Mars surface show regional variations in their Mg/(Mg + Fe) ratio (Mg#). The clear boundary we observe between the two types of crust in our geological mapping (respectively, red and orange in Figure 13) could be related to the limit between lava flows issued from two slightly different mantle sources or emplaced at different stages of differentiation. These two units would have been excavated without distinction during later impact processes.

[63] Later in the regional history, around the Noachian/Hesperian transition, the Syrtis Major volcanic edifice started to form. The peripheral unit, the oldest lavas that are accessible nowadays, emplaced at high temperatures, as indicated by the Mg-rich composition of the pyroxenes. In this case, olivine is not detected with our spectroscopic analysis but could be present in proportions of less than 20% [*Clenet et al*., 2011]. Temperatures above 1200°C would lead to lava flows with very low viscosities, which are typically expected for such a shield volcano shape. During the latest stage of Syrtis Major formation, around early to middle Hesperian [*Hiesinger and Head*, 2004], the magmatic reservoir had cooled enough to differentiate silica-rich compositions corresponding to crystallization along the two pyroxenes cotectic. Olivine crystallization in this latest phase could be explained either by a local process directly related to the evolution of the magma chamber or by a broader-scale change where global early Hesperian volcanism would be olivine enriched, as proposed by *Ody et al*. [2013].

#### 5.5.4. Syrtis Major Rocks and Relations With Other Observations

[64] Iron contents deduced from our spectroscopic approach are consistent for all the different parts of the volcanic edifice and for all the three mafic minerals. The actual range of Mg#, between 50 and 80, is also consistent with previous observations like the ones done on basalts in Gusev crater [*McSween et al*., 2006] and analyses on SNCs [*McSween and Treiman*, 1998; *Meyer*, 2003, and references therein]. However, due to our inability at detecting spectral signature of plagioclase or glass when mixed with mafic materials, we are not able to estimate an exact bulk modal composition. A side effect is that a particular unit such as the dacite unit proposed by *Christensen et al*. [2005] using TES data is mapped here in the HCP unit. This should, however, marginally affect our results as such a specific unit has not been detected elsewhere.

[65] The variations in pyroxene and olivine contents we deduce from the orbital data can nevertheless be compared to the modal composition of Martian meteorites. Basaltic shergottites have very little or no olivine and a high-pigeonite content. This does not fit with our observations. Conversely, both basalts in Gusev crater and olivine-phyric shergottites have larger amount of olivine than what we observe in the case of Syrtis Major lava flows. A possible explanation could be related to weathering processes, which could have altered olivine preferentially compared to pyroxenes. This would also imply an environmental change between the two stages of Syrtis Major emplacement as we detect more olivine in the central lavas than in the peripheral areas. The central lavas unit exhibits compositions which could also be compared to nakhlites. Those meteorites are composed mostly of augite with some olivine and, in the case of NWA998, some low-Ca pyroxene [*Treiman*, 2005]. It has already been proposed that these meteorites come from the Syrtis Major area [*Harvey and Hamilton*, 2005]. However, pyroxenes in nakhlites are more iron rich than what we deduce from orbital data. There also is a discrepancy between the nakhlites crystallization ages and Syrtis Major dating from crater counting. Thus, it appears that to date, none of the SNC compositions perfectly match with our results at Syrtis Major.

## 6. Conclusion

[66] In this study, we used a systematic MGM approach developed by *Clenet et al*. [2011] to process large hyperspectral data sets. We first demonstrate the ability of this new MGM approach to map lithological units in mafic terranes in a controlled case study on Earth, i.e., the Sumail massif in the Oman ophiolite, where we conducted an airborne hyperspectral survey with the HyMap instrument. We were able to clearly distinguish between the mantle section which is harzburgite dominated (olivine + LCP) and the crustal section which is mainly made of HCP-rich (+variable olivine content) cumulates (gabbros, troctolites, pyroxenites, wehrlites). MGM results have also enhanced subtle spectroscopic variations which can be directly related to weak but regionally significant variations in pyroxenes iron or calcium content. These results have been validated by field and petrologic work and indicate that our approach is valid for mapping extraterrestrial surfaces.

[67] We then charted the various mafic assemblages across the Syrtis Major volcanic shield on Mars using an integrated VNIR-SWIR OMEGA/MEx mosaic. Our results are in agreement with previous work; however, olivine appears to be more abundant than previously considered in the central part of the volcanic edifice, especially in ternary mafic assemblages involving orthopyroxene (enstatite), clinopyroxene (augite), and olivine. This particular area also correlates with earlier observations from thermal infrared data. No obvious link between morphology and mineralogy has been found. We propose that the variations found in the olivine and pyroxenes chemical compositions are related to igneous processes, putting new constraints on the Syrtis Major regional history. Regional variations in mineral assemblages and pyroxene compositions help infer ranges of crystallization temperatures and/or magma source composition. Although our petrologic model is far from being unique, our data are consistent with a progressive evolution of the magmatic composition, possibly related to the thermal history of the area as the ancient crust and subsequent lava flows are emplaced, and call for further petrologic studies [e.g., *Baratoux et al*., 2013]. Increase of olivine content in the central part of the volcanic edifice is interpreted as a later episode of eruption of Mg-rich, high-temperature magma.

[68] **Acknowledgments.** This project was supported by the French Space Agency CNES and PNP (Programme National de Planétologie) and has benefited from the scientific environment of Paul Sabatier University (Toulouse). Harold Clenet has also benefited of a PhD grant funded by the French Ministry of Education. Financial and technical support was provided by the Centre National de la Recherche Scientifique (France). Authors are very grateful to the whole OMEGA team for the excellent job done. We express our warm thanks to J. Sunshine and J. R. Skok whose painstaking editing corrections, thorough comments, and suggestions greatly contributed to improve the manuscript.

## References


Adams, J. B. (1968), Lunar and Martian surfaces: Petrologic significance of absorption bands in the near-infrared, *Science*, *159*, 1453–1455.

Adams, J. B. (1974), Visible and near IR diffuse reflectance spectra of pyroxenes as applied to remote sensing of solid objects in the solar system, *J. Geophys. Res.*, *79*(32), 4829–4836.

Adams, J. B. (1975), Interpretation of visible and near-infrared diffuse reflectance spectra of pyroxenes and other rock forming minerals, in *Infrared and Raman Spectroscopy of Lunar and Terrestrial Materials*, edited by C. Karr, pp. 91–116, Academic, New York.

Amri, I. (1995), Etude pétrologique et structurale d'une dorsale océanique fossile, Massif de Sumail (ophiolite d'Oman). Implications pour les mécanismes d'accrétion océanique, 199 pp., Toulouse University.

Bandfield, J. L. (2002), Global mineral distributions on Mars, *J. Geophys. Res.*, *107*(E6), 5042, doi:10.1029/2001JE001510.

Bandfield, J. L., V. E. Hamilton, and P. R. Christensen (2000), A global view of Martian surface compositions from MGS-TES, *Science*, *287*, 1626–1630.

Baratoux, D., N. Mangold, P. C. Pinet, and F. Costard (2005), Thermal properties of lobate ejecta in Syrtis Major, Mars: Implications for the mechanisms of formation, *J. Geophys. Res.*, *110*, E04011, doi:10.1029/2004JE002314.

Baratoux, D., P. C. Pinet, A. Gendrin, L. C. Kanner, J. F. Mustard, Y. Daydou, J. Vaucher, and J.-P. Bibring (2007), Mineralogical structure of the subsurface of Syrtis Major from OMEGA observations of lobate ejecta blankets, *J. Geophys. Res.*, *112*, E08S05, doi:10.1029/2007JE002890.

Baratoux, D., M. J. Toplis, M. Monnereau, and O. Gasnault (2011), Thermal history of Mars inferred from orbital geochemistry of volcanic provinces, *Nature*, *472*, 338–342, doi:10.1038/nature09903.

Baratoux, D., M. J. Toplis, M. Monnereau, and V. Sautter (2013), The petrological expression of early Mars volcanism, *J. Geophys. Res. Planets*, *118*, 1–6, doi:10.1029/2012JE004234.

Bell, J. F., M. J. Wolff, P. B. James, R. T. Clancy, S. W. Lee, and L. J. Martin (1997), Mars surface mineralogy from Hubble Space Telescope imaging during 1994–1995: Observations, calibration, and initial results, *J. Geophys. Res.*, *102*, 9109–9123.

Bellucci, G., F. Altieri, J.-P. Bibring, G. Bonello, Y. Langevin, B. Gondet, and F. Poulet (2006), OMEGA/Mars Express: Visual channel performances and data reduction techniques, *Planet. Space Sci.*, *54*, 675–684, doi:10.1016/j.pss.2006.03.006.

Benoit, M., G. Ceuleneer, and M. Polvé (1999), The remelting of hydrothermally altered peridotite at mid-ocean ridges by intruding mantle diapirs, *Nature*, *402*, 514–518.

Bibring, J.-P., and S. Erard (2001), The Martian surface composition, *Space Sci. Rev.*, *96*(1–4), 293–316.

Bibring, J.-P., et al. (2004), OMEGA: Observatoire pour la Minéralogie, L'Eau, les Glaces et l'Activité, ESA Special publications, SP-1240.

Bibring, J.-P., et al. (2005), Mars surface diversity as revealed by the OMEGA/Mars Express observations, *Science*, *307*, 1576–1581, doi:10.1126/science.1108806.

Bibring, J.-P., et al. (2006), Global mineralogical and aqueous Mars history derived from OMEGA/Mars Express data, *Science*, *312*, 400–404, doi:10.1126/science.1122659.

Boardman, J. W. (1998), Post-ATREM polishing of AVIRIS apparent reflectance data using EFFORT: A lesson in accuracy versus precision, in *Summaries of the Seventh JPL Airborne Earth Science Workshop*, p. 53, JPL publications 97-21.

Bonello, G., J.-P. Bibring, A. Soufflot, Y. Langevin, B. Gondet, M. Berthé, and C. Carabetian (2005), The ground calibration setup of OMEGA and VIRTIS experiments: Description and performances, *Planet. Space Sci.*, *53*(7), 711–728, doi:10.1016/j.pss.2005.02.002.

Burns, R. G. (1970), Crystal field spectra and evidence of cation ordering in olivine minerals, *Am. Mineral.*, *55*, 1608–1632.

Burns, R. G. (1993), *Mineralogical Applications of Crystal Field Theory*, 2nd ed., Cambridge University Press, Cambridge, UK.

Carrozzo, F. G., F. Altieri, G. Bellucci, F. Poulet, E. D'Aversa, and J.-P. Bibring (2012), Iron mineralogy of the surface of Mars from the 1 μm band spectral properties, *J. Geophys. Res.*, *117*, E00J17, doi:10.1029/2012JE004091.

Ceuleneer, G. (1991), Evidence for a paleo-spreading center in the Oman ophiolite: Mantle structures in the Maqsad area, in *Ophiolite Genesis and Evolution of Oceanic Lithosphere*, edited by T. J. Peters, pp. 149–175, Kluwer Academic Press, Dordrecht, the Netherlands.

Ceuleneer, G., A. Nicolas, and F. Boudier (1988), Mantle flow pattern at an oceanic spreading centre: The Oman peridotite record, *Tectonophysics*, *151*, 1–26.

Ceuleneer, G., M. Monnereau, and I. Amri (1996), Thermal structure of a fossil mantle diapir inferred from the distribution of mafic cumulates, *Nature*, *379*, 149–153.

Chabrillat, S., P. C. Pinet, G. Ceuleneer, P. E. Johnson, and J. F. Mustard (2000), Ronda peridotite massif: Methodology for its geological mapping and lithological discrimination from airborne hyperspectral data, *Int. J. Remote Sens.*, *21*(12), 2363–2388.

Christensen, P. R., et al. (2005), Evidence for magmatic evolution and diversity on Mars from infrared observations, *Nature*, *436*, 504–509, doi:10.1038/nature03639.

Clenet, H. (2009), Télédétection hyperspectrale: minéralogie et pétrologie, Application au volcan Syrtis Major (Mars) et à l'ophiolite d'Oman, 362 pp., Toulouse University.

Clenet, H., P. C. Pinet, Y. Daydou, F. Heuripeau, C. Rosemberg, and G. Ceuleneer (2008), A systematic testing approach using the Modified Gaussian Model (MGM) for mafic mineralogy mapping in natural conditions (Earth, Mars), in *Lunar and Planetary Science Conference*, p. 1918, Lunar and Planetary Institute, Houston, TX.

Clenet, H., G. Ceuleneer, P. C. Pinet, B. Abily, Y. Daydou, and C. Dantas (2010), Thick sections of layered ultramafic cumulates in the Oman ophiolite revealed by an airborne hyper-spectral survey: Petrogenesis and relationship to mantle diapirism, *Lithos*, *114*, 265–281, doi:10.1016/j.lithos.2009.09.002.

Clenet, H., P. C. Pinet, Y. Daydou, F. Heuripeau, C. Rosemberg, D. Baratoux, and S. Chevrel (2011), A new systematic approach using the Modified Gaussian Model: Insight for the characterization of chemical composition of olivines, pyroxenes and olivine–pyroxene mixtures, *Icarus*, *213*, 404–422, doi:10.1016/j.icarus.2011.03.002.

Clenet, H., C. Quantin, M. Andréani, X. Ceamanos, P. Allemand, and P. C. Pinet (2012), Noachian crust composition and early alteration processes in the vicinity of Valles Marineris as seen from the central peaks of impact craters, in *Third Early Mars Conference*, p. 7026, Lunar and Planetary Institute, Houston, TX.

Cloutis, E. A., and M. J. Gaffey (1991a), Pyroxene spectroscopy revisited: Spectral-compositional correlations and relationship to geothermometry, *J. Geophys. Res.*, *96*, 22,809–822,826.

Cloutis, E. A., and M. J. Gaffey (1991b), Spectral-compositional variations in the constituent minerals of mafic and ultramafic assemblages and remote sensing implications, *Earth, Moon, Planets*, *53*(1), 11–53.

Cloutis, E. A., M. J. Gaffey, T. L. Jackowski, and K. L. Reed (1986), Calibrations of phase abundance, composition, and particle size distribution for olivine-orthopyroxene mixtures from reflectance spectra, *J. Geophys. Res.*, *91*, 11,611–641,653.

Cocks, T., R. Jenssen, A. Stewart, I. Wilson, and T. Shields (1998), The HyMap airborne hyperspectral sensor: The system, calibration and performance, in *1st EARSEL Workshop on Imaging Spectroscopy*, European Association of Remote Sensing Laboratories, Zurich.

Combe, J.-P., P. Launeau, P. C. Pinet, D. Despan, E. Harris, G. Ceuleneer, and C. Sotin (2006), Mapping of an ophiolite complex by high-resolution visible-infrared spectrometry, *Geochem. Geophys. Geosyst.*, *7*, Q08001, doi:10.1029/2005GC001214.

Combe, J.-P., et al. (2008), Analysis of OMEGA/Mars Express data hyperspectral data using a Multiple-Endmember Linear Spectral Unmixing Model (MELSUM): Methodology and first results, *Planet. Space Sci.*, *56*, 951–975, doi:10.1016/j.pss.2007.12.007.

Cooperative Institute for Research in Environmental Sciences (1999), CIRES Atmosphere Removal Program (ATREM), User's Guide, Version 3.1, Boulder.

Dyar, M. D., et al. (2009), Spectroscopic characteristics of synthetic olivine: An integrated multi-wavelength and multi-technique approach, *Am. Mineral.*, *94*(7), 883–898, doi:10.2138/am.2009.3115.

Ehlmann, B. L., and J. F. Mustard (2012), An in-situ record of major environmental transitions on early Mars at Northeast Syrtis Major, *Geophys. Res. Lett.*, *39*, L11202, doi:10.1029/2012GL051594.

Ehlmann, B. L., et al. (2009), Identification of hydrated silicate minerals on Mars using MRO-CRISM: Geologic context near Nili Fossae and implications for aqueous alteration, *J. Geophys. Res.*, *114*, E00D08, doi:10.1029/2009JE003339.

Gao, B.-C. B.-C., K. B. Heidebrecht, and A. F. H. Goetz (1993), Derivation of scaled surface reflectances from AVIRIS data, *Remote Sens. Environ.*, *44*, 165–178.

Glennie, K. W., M. G. A. Boeuf, M. W. H. Clarke, M. Moody-Stuart, W. F. H. Pilaar, and T. M. Reinhard (1974), Geology of the Oman mountains, *K. Ned. Geol. Mijnbouwkundig Genootschap*, *31*, 423.

Greeley, R., and J. E. Guest (1987), Geological map of the eastern equatorial region of Mars, Map I-1802-B, Scale 1:15,000,000.

Greeley, R., and P. D. Spudis (1981), Volcanism on Mars, *Rev. Geophys. Space Phys.*, *19*(1), 13–41, doi:10.1029/RG019i001p00013.

Hamilton, V. E., and P. R. Christensen (2005), Evidence for extensive, olivine-rich bedrock on Mars, *Geology*, *33*(6), 433–436, doi:10.1130/G21258.1.

Hamilton, V. E., M. B. Wyatt, H. Y. McSween Jr., and P. R. Christensen (2001), Analysis of terrestrial and Martian volcanic compositions using thermal emission spectroscopy. Application to Martian surface spectra from the Mars Global Surveyor Thermal Emission Spectrometer, *J. Geophys. Res.*, *106*, 14,714–733,746.

Hamilton, V. E., P. R. Christensen, H. Y. McSween, and J. L. Bandfield (2003), Searching for the source regions of Martian meteorites using MGS TES: Integrating Martian meteorites into the global distribution of igneous materials on Mars, *Meteorit. amp. Planet. Sci.*, *38*(6), 871–885.

Hartmann, W. K., and G. Neukum (2001), Cratering chronology and the evolution of Mars, *Space Sci. Rev.*, *96*, 165–194.

Harvey, R. P., and V. E. Hamilton (2005), Syrtis Major as the source region of the Nakhlite/Chassigny group of martian meteorites: Implications for the geological history of Mars, in *Lunar and Planetary Science Conference*, vol. 7216, p. 1019, Lunar and Planetary Institute, Houston, TX.

Hazen, R. M., P. M. Bell, and H. K. Mao (1978), Effects of compositional variation on absorption spectra of lunar pyroxenes, in *Proceedings of the Lunar and Planetary Science Conference 9th*, pp. 2919–2934, Lunar and Planetary Institute, Houston, TX.

Hiesinger, H., and J. W. Head (2004), The Syrtis Major volcanic province, Mars: Synthesis from Mars Global Surveyor data, *J. Geophys. Res.*, *109*, E01004, doi:10.1029/2003JE002143.

Hoefen, T. M., R. N. Clark, J. L. Bandfield, M. D. Smith, J. C. Pearl, and P. R. Christensen (2003), Discovery of olivine in the Nili Fossae region of Mars, *Science*, *302*, 627–630.

Hunt, G. R. (1977), Spectral signatures of particulate minerals in the visible and near infrared, *Geophysics*, *42*, 501–513.

Hunt, G. R., and J. W. Salisbury (1970), Visible and near infrared spectra of minerals and rocks, I, silicate minerals, *Mod. Geol.*, *1*, 283–300.

Kanner, L. C., J. F. Mustard, and A. Gendrin (2007), Assessing the limits of the Modified Gaussian Model for remote spectroscopic studies of pyroxenes on Mars, *Icarus*, *187*, 442–456, doi:10.1016/j.icarus.2006.10.025.

King, T. V. V., and W. I. Ridley (1987), Relation of the spectroscopic reflectance of olivine to mineral chemistry and some remote sensing implications, *J. Geophys. Res.*, *92*, 11,411–457,469.

Klima, R. L., C. M. Pieters, and M. D. Dyar (2007), Spectroscopy of synthetic Mg-Fe pyroxenes I: Spin-allowed and spin-forbidden crystal field bands in the visible and near-infrared, *Meteorit. Planet. Sci.*, *42*(2), 235–253.

Klima, R. L., M. D. Dyar, and C. M. Pieters (2011), Near-infrared spectra of clinopyroxenes: Effects of calcium content and crystal structure, *Meteorit. Planet. Sci.*, *46*(3), 379–395, doi:10.1111/j.1945-5100.2010.01158.x.

Koeppen, W. C., and V. E. Hamilton (2008), Global distribution, composition, and abundance of olivine on the surface of Mars from thermal infrared data, *J. Geophys. Res.*, *113*, E05001, doi:10.1029/2007JE002984.

Langevin, Y., F. Poulet, J.-P. Bibring, and B. Gondet (2005), Sulfates in the north polar region of Mars detected by OMEGA/Mars Express, *Science*, *307*(5715), 1584–6, doi:10.1126/science.1109091.

Lindsley, D. H. (1983), Pyroxene thermometry, *Am. Mineral.*, *68*, 477–493.

Mangold, N., D. Baratoux, O. Arnalds, J.-M. Bardintzeff, B. Platevoet, M. Grégoire, and P. C. Pinet (2011), Segregation of olivine grains in volcanic sands in Iceland and implications for Mars, *Earth Planet. Sci. Lett.*, *310*, 233–243, doi:10.1016/j.epsl.2011.07.025.

McCoy, T. J., G. J. Taylor, and K. Keil (1992), Zagami: Product of a two-stage magmatic history, *Geochim. Cosmochim. Acta*, *56*, 3571–3582.

McSween, H. Y. (1994), What we have learned about Mars from SNC meteorites, *Meteorit. Planet. Sci.*, *29*, 757–779.

McSween, H. Y., and A. H. Treiman (1998), Martian samples, in *Planetary Materials. Reviews in Mineralogy*, *Vol. 36*, edited by J. J. Papike, pp. 6–01, 6–54, Mineralogical Society of America, Washington.

McSween, H. Y., et al. (2006), Characterization and petrologic interpretation of olivine-rich basalts at Gusev Crater, Mars, *J. Geophys. Res.*, *111*, E02S10, doi:10.1029/2005JE002477.

Meyer, C. (2003), *Mars Meteorite Compendium*, Johnson Space Center, Houston, TX.

Mittlefehldt, D. W. (1994), ALH84001, a cumulate orthopyroxenite member of the Martian meteorite clan, *Meteorit. amp. Planet. Sci.*, *29*, 214–221.

Mustard, J. F., and J. M. Sunshine (1995), Seeing through the dust: Martian crustal heterogeneity and links to the SNC meteorites, *Science*, *267*(5204), 1623–1626.

Mustard, J. F., S. Erard, J.-P. Bibring, J. W. Head, S. Hurtrez, Y. Langevin, C. M. Pieters, and C. Sotin (1993), The surface of Syrtis Major: Composition of the volcanic substrate and mixing with altered dust and soil, *J. Geophys. Res.*, *98*, 3387–3400.

Mustard, J. F., S. L. Murchie, S. Erard, and J. M. Sunshine (1997), In situ compositions of Martian volcanics: Implications for the mantle, *J. Geophys. Res.*, *102*, 25,605–625,615.

Mustard, J. F., F. Poulet, A. Gendrin, J.-P. Bibring, Y. Langevin, B. Gondet, N. Mangold, G. Bellucci, and F. Altieri (2005), Olivine and pyroxene diversity in the crust of Mars, *Science*, *307*(5715), 1594–1597, doi:10.1126/science.1109098.

Mustard, J. F., F. Poulet, J. W. Head, N. Mangold, J.-P. Bibring, S. M. Pelkey, C. I. Fassett, Y. Langevin, and G. Neukum (2007), Mineralogy of the Nili Fossae region with OMEGA/Mars Express data: 1. Ancient impact melt in the Isidis Basin and implications for the transition from the Noachian to Hesperian, *J. Geophys. Res.*, *112*, E08S03, doi:10.1029/2006JE002834.

Mustard, J. F., B. L. Ehlmann, S. L. Murchie, F. Poulet, N. Mangold, J. W. Head, J.-P. Bibring, and L. H. Roach (2009), Composition, morphology, and stratigraphy of Noachian crust around the Isidis basin, *J. Geophys. Res.*, *114*, E00D12, doi:10.1029/2009JE003349.

Ody, A., F. Poulet, Y. Langevin, J.-P. Bibring, G. Bellucci, F. Altieri, B. Gondet, M. Vincendon, J. Carter, and N. Manaud (2012), Global maps of anhydrous minerals at the surface of Mars from OMEGA/MEx, *J. Geophys. Res.*, *117*, 1–14, doi:10.1029/2012JE004117.

Ody, A., F. F. Poulet, J.-P. Bibring, D. Loizeau, J. Carter, B. Gondet, and Y. Langevin (2013), Global investigation of olivine on Mars: Insights into crust and mantle compositions, *J. Geophys. Res. Planet*, *118*(October 2012), 1–29, doi:10.1029/2012JE004149.

Pinet, P. C., and S. Chevrel (1990), Spectral identification of geological units on the surface of Mars related to the presence of silicates from Earth-based near-infrared telescopic charge-coupled device imaging, *J. Geophys. Res.*, *95*, 14,414–435,446.

Pinet, P. C., et al. (2003), Hyperspectral remote sensing approach for rock surface mineralogy mapping in arid environment, in *IUGG XXXIII General Assembly*, Int. Union of Geod. and Geophys, Sapporo, Japan.

Pinet, P. C., et al. (2006), Mantle rock surface mineralogy mapping in arid environment from imaging spectroscopy: The case of the Maqsad peridotitic massif in Oman and implications for the spectroscopic study of exposed mafic units on Mars, in *Lunar and Planetary Science Conference*, p. 1346, Lunar and Planetary Institute, Houston, TX.

Pinet, P. C., et al. (2007), Mafic mineralogy variations across Syrtis Major shield and surroundings as inferred from visible-near-infrared spectroscopy by OMEGA/Mars Express, in *7th Mars Conference, Pasadena*, p. 3146, Lunar and Planetary Institute, Houston, TX.

Poulet, F., N. Mangold, and S. Erard (2003), A new view of dark Martian regions from geomorphic and spectroscopic analysis of Syrtis Major, *Astron. Astrophys.*, *412*, L19–L23, doi:10.1051/0004-6361:20031661.

Poulet, F., C. Gomez, J.-P. Bibring, Y. Langevin, B. Gondet, P. C. Pinet, G. Bellucci, and J. F. Mustard (2007), Martian surface mineralogy from Observatoire pour la Minéralogie, l'Eau, les Glaces et l'Activité on board the Mars Express spacecraft (OMEGA/MEx): Global mineral maps, *J. Geophys. Res.*, *112*, E08S02, doi:10.1029/2006JE002840.

Poulet, F., et al. (2009), Quantitative compositional analysis of Martian mafic regions using the MEx/OMEGA reflectance data: 2. Petrological implications, *Icarus*, *201*(1), 84–101, doi:10.1016/j.icarus.2008.12.042.

Python, M., and G. Ceuleneer (2003), Nature and distribution of dykes and related melt migration structures in the mantle section of the Oman ophiolite, *Geochem. Geophys. Geosyst.*, *4*(7), 8612, doi:10.1029/2002GC000354.

Rabinowicz, M., and G. Ceuleneer (2005), The effect of sloped isotherms on melt migration in the shallow mantle: A physical and numerical model based on observations in the Oman ophiolite, *Earth Planet. Sci. Lett.*, *229*(3–4), 231–246, doi:10.1016/j.epsl.2004.09.039.

Rabu, D., P. Nehlig, and J. Roger (1986), Geological map of Nakhl, Sheet NF 40-3E, Scale 1:100,000, Explanatory Notes.

Reyes, D. P., and P. R. Christensen (1994), Evidence for Komatiite-type lavas on Mars from Phobos ISM data and other observations, *Geophys. Res. Lett.*, *21*, 887–890.

Rogers, A. D., and P. R. Christensen (2007), Surface mineralogy of Martian low-albedo regions from MGS-TES data: Implications for upper crustal evolution and surface alteration, *J. Geophys. Res.*, *112*, E01003, doi:10.1029/2006JE002727.

Roy, R., P. Launeau, V. Carrère, G. Ceuleneer, H. Clenet, P. C. Pinet, Y. Daydou, J. Girardeau, and I. Amri (2009), Geological mapping strategy using VNIR hyperspectral remote sensing: Application to the Oman ophiolite (Sumail Massif), *Geochem. Geophys. Geosyst.*, *10*, Q02004, doi:10.1029/2008GC002154.

Schaber, G. G. (1982), Syrtis Major: A low-relief volcanic shield, *J. Geophys. Res.*, *87*, 9852–9866.

Singer, R. B. (1981), Near-infrared spectral reflectance of mineral mixtures: Systematic combinations of pyroxenes, olivine and iron oxides, *J. Geophys. Res.*, *86*, 7967–7982.

Skok, J. R., J. F. Mustard, B. L. Ehlmann, R. E. Milliken, and S. L. Murchie (2010a), Silica deposits in the Nili Patera caldera on the Syrtis Major volcanic complex on Mars, *Nat. Geosci.*, *3*, 838–841, doi:10.1038/NGEO990.

Skok, J. R., J. F. Mustard, S. L. Murchie, M. B. Wyatt, and B. L. Ehlmann (2010b), Spectrally distinct ejecta in Syrtis Major, Mars: Evidence for environmental change at the Hesperian-Amazonian boundary, *J. Geophys. Res.*, *115*, E00D14, doi:10.1029/2009JE003338.

Skok, J. R., J. F. Mustard, L. L. Tornabene, C. Pan, A. D. Rogers, and S. L. Murchie (2012), A spectroscopic analysis of Martian crater central peaks: Formation of the ancient crust, *J. Geophys. Res.*, *117*, E00J18, doi:10.1029/2012JE004148.

Smith, J. V., and R. L. Hervig (1979), Shergotty meteorite: Mineralogy, petrography and minor elements, *Meteorit. Planet. Sci.*, *14*, 121–141.

Stolper, E. M., and H. Y. McSween (1979), Petrology and origin of the shergottite meteorites, *Geochim. Cosmochim. Acta*, *43*(9), 1475–1477.

Sunshine, J. M., and C. M. Pieters (1993), Estimating modal abundances from the spectra of natural and laboratory pyroxene mixtures using the modified Gaussian model, *J. Geophys. Res.*, *98*, 9075–9087.

Sunshine, J. M., and C. M. Pieters (1998), Determining the composition of olivine from reflectance spectroscopy, *J. Geophys. Res.*, *103*, 13,613–675,688.

Sunshine, J. M., C. M. Pieters, and S. F. Pratt (1990), Deconvolution of mineral absorption bands: An improved approach, *J. Geophys. Res.*, *93*, 6955–6966.

Treiman, A. H. (2005), The nakhlite meteorites: Augite-rich igneous rocks from Mars, *Chem. der Erde Geochem.*, *65*(3), 203–270, doi:10.1016/j.chemer.2005.01.004.

Villey, M., J. Le Métour, and X. De Gramont (1986), Geological map of Fanjah, s

Viviano, C. E., and J. E. Moersch (2012), A technique for mapping Fe/Mg-rich phyllosilicates on Mars using THEMIS multispectral thermal infrared images, *J. Geophys. Res.*, *117*, 1–15, doi:10.1029/2011JE003985.